Computer Methods in Applied Mechanics and Engineering 461 (2026) 119154

Contents lists available at ScienceDirect

Comput. Methods Appl. Mech. Engrg.

journal homepage: www.elsevier.com/locate/cma

Bridging hydrodynamics and granulation kinetics: An efficient 2D CFD-coupled compartmental PBM approach for fluidised bed granulation

Zeeshan Ansari [a], Mainendra Kumar Dewangan [b,*], Ashok Das [c,*], Stefan Heinrich [d], Rohit Ramachandran [e], Mehakpreet Singh [a,b,**]

[a] Mathematics Applications Consortium for Science and Industry (MACSI), Department of Mathematics and Statistics, University of Limerick, Limerick V94 T9PX, Ireland
[b] Bernal Institute, University of Limerick, Limerick V94 T9PX, Ireland
[c] Department of Mathematics and Computing, Indian Institute of Technology (ISM), Dhanbad, Jharkhand, 826004, India
[d] Institute of Solids Process Engineering and Particle Technology, Hamburg University of Technology, Denickestraße 15, 21073, Hamburg, Germany
[e] Chemical and Biochemical Engineering, Rutgers University, 98 Brett Road, Piscataway, NJ, 08854, USA

ARTICLE INFO

Keywords:
Wet sprayed fluidised granulation
Computational fluid dynamics
Population balance model
Coupled modelling
Particle size distribution
Finite volume scheme

ABSTRACT

Spray fluidised bed granulation (SFBG) is a widely used technology in the pharmaceutical, agricultural, and chemical industries to produce granules with controlled particle-size distributions (PSD) and enhanced functional properties. The present study develops an efficient coupled computational fluid dynamics (CFD)-population balance model (PBM) to optimise the SFBG process. A compartmental modelling strategy is employed to capture the evolution of PSD resulting from aggregation and breakage mechanisms in the wetting and drying compartments, respectively. The CFD model adopts an Eulerian–Eulerian formulation in a two-dimensional (2D) computational domain to estimate particle exchange rates between compartments. The two-compartment PBM is solved using a two-moment-preserving finite-volume scheme. The predictions of the present study are compared against available experimental results and previously reported computational studies. The 2D CFD model reproduces the expected pressure-drop behaviour and shows bed-expansion behaviour comparable to the reported 3D CFD results, while reducing computational cost. Within the PBM framework, several aggregation kernels are evaluated to optimise the PSD. Sensitivity analysis indicates that the size-dependent generalised shear aggregation kernel provides superior predictive performance compared with the Kapur, Brownian and other kernels. Overall, the proposed 2D coupled CFD–PBM modelling offers an accurate and computationally efficient approach for modelling and optimisation of the SFBG process compared with the existing model.

* Corresponding authors.
** Corresponding author at: Mathematics Applications Consortium for Science and Industry (MACSI), Department of Mathematics and Statistics, University of Limerick, Limerick V94 T9PX, Ireland.
E-mail addresses: ansari.zeeshan@ul.ie (Z. Ansari), mainendra.dewangan@ul.ie (M.K. Dewangan), ashokdas@iitism.ac.in (A. Das), stefan.heinrich@tuhh.de (S. Heinrich), rohit.r@rutgers.edu (R. Ramachandran), mehakpreet.singh@ul.ie (M. Singh).

https://doi.org/10.1016/j.cma.2026.119154
Received 9 April 2026; Received in revised form 1 June 2026; Accepted 5 June 2026
Available online 18 June 2026

1. Introduction

Granulation is a key unit operation widely used across manufacturing industries, including agriculture, food, pharmaceutical, and chemicals. The process improves key particle properties, including porosity, compressibility, and mechanical strength, thereby enhancing flowability, drying behaviour, mixing, and overall processability [1]. The granulation technique is primarily implemented using two methods: wet granulation and dry granulation [2,3]. As indicated by its name, wet granulation employs a binder liquid that is sprayed to agitate powder particles, facilitating their cohesion through a combination of capillary forces and viscous interactions [4]. Following this process, the solvent is removed by evaporation during the drying phase, allowing the formation of more stable bonds. The strength of the resulting granules is largely attributed to solid bridges created by the hardening of the binder and the crystallisation of dissolved particles. Conversely, dry granulation methods rely on the compaction of the powder mass, followed by crushing and sieving to achieve the desired particle size enlargement. This approach does not utilise a binder liquid, making it particularly advantageous for formulations containing moisture- or heat-sensitive active pharmaceutical ingredients. While both methods have their applications, wet granulation generally provides superior control over drug content uniformity, product bulk density, and overall compatibility [5].

Spray fluidised bed granulation (SFBG) is a wet granulation process, and it has several applications in the field of particle technology such as agricultural, food, and chemical industries for producing granules with controlled particle-size distributions (PSD) and improved product functionality. Despite decades of industrial applications, improving the efficiency, predictive capability, and operational control of SFBG remains a central focus of research [6–11]. In an SFBG system (refer Fig. 1), a fine powder bed is fluidised by a stream of hot gas introduced at the base of the chamber, enabling the particles to circulate freely in a fluidised state. For a top spray SFBG, liquid binder is atomised onto the suspended particles through spray nozzles located at the top of the chamber. The simultaneous wetting and drying processes within the system initiate phenomena such as aggregation (particle–particle coalescence due to binder-induced adhesion) and breakage (fragmentation of larger agglomerates due to particle–particle and particle–wall collisions), which collectively facilitate the formation and evolution of granules towards a more uniform size distribution [4,12].

The internal dynamics of SFBG are inherently complex, arising from the concurrent interaction of multiphase flow, spray atomisation, particle–particle collisions, aggregation, and breakage [13]. Capturing these coupled mechanisms is crucial to predicting the evolution of the PSD. However, predictive modelling of SFBG remains challenging because multiple competing time scales govern the process, including liquid deposition and spreading, particle drying, collision frequency, and the residence time of particles within different regions of the bed [4]. Moreover, SFBG exhibits strong spatial heterogeneity: the vicinity of the spray zone, dense bed, and freeboard can differ substantially in solids holdup, temperature, and humidity, leading to region-dependent wetting and drying histories [14]. As a result, the same operating condition may yield different local aggregation and breakage tendencies, complicating the identification of representative rate expressions from global PSD measurements alone [15].

In population balance models (PBMs), these rate expressions are typically embedded in the aggregation and breakage kernels that strongly influence the PSD predictions [15]. Classical PBMs have therefore been widely used to describe the PSD dynamics in SFBG, as they provide a mathematical framework for representing aggregation, breakage, nucleation, and growth mechanisms. Nevertheless, these approaches often rely on a well-mixed assumption of the system [16,17], whereby the aggregation and breakage are treated as spatially homogeneous throughout the bed. This limits their ability to account for heterogeneity in the temperature, humidity, and particle motion within the mixed-bed. On the other hand, the computational fluid dynamics (CFD) approach provides a mechanistic framework for resolving gas–solid hydrodynamics, interphase momentum exchange, and heat and mass transfer, thereby capturing local flow structures and non-uniformities that are absent in PBM-based approaches [18]. However, CFD alone cannot resolve the PSD, as temporal evolution of PSD are not inherently embedded within the CFD governing equations.

To address these challenges in the literature, numerous CFD–PBM coupling methodologies have been proposed [9,19–21], each offering distinct advantages and limitations. Broadly, these strategies can be classified into integrated approaches, in which PBM is solved directly within the CFD solver, and stand-alone approaches, in which CFD provides hydrodynamic fields to a separate PBM solver [9,22]. Coupling strategies can be distinguished by their degree of feedback. In the simplest one-way configuration, the CFD supplies flow properties to PBM without feedback, while the two-way coupling incorporates the PBM predictions back into the CFD solution. In CFD–PBM research, integrated two-way coupling is typically seen as computationally intensive, whereas stand-alone one-way coupling provides flexibility and efficiency, making it a popular option for quick parametric analyses and optimisation [9,10]. In addition to the coupling strategy, the dimensionality of the CFD model significantly affects both prediction accuracy and computational cost. Three-dimensional (3D) CFD is widely used in CFD–PBM studies of fluidised-bed granulation because it provides a higher degree of detail in the representation of bubble dynamics, voidage distribution, and wall effects [23]. In contrast, two-dimensional (2D) CFD simulations are computationally efficient. However, these efficiency gains come at the expense of accuracy: 2D models often exaggerate bubble coalescence, bed pressure drop, and wall effects, limiting their ability to resolve complex flow variation [24]. Therefore, 2D models are more appropriate for preliminary investigations and early design stages, with rigorous validation required before extending them to CFD–PBM applications.

CFD–PBM frameworks are strongly influenced by the numerical method used to solve the PBM. Over the past few decades, significant work has focused on improving the representation of particle aggregation, breakage, nucleation and growth by employing various numerical techniques while maintaining computational efficiency [19,25,26]. The key difference among these formulations lies in the discretisation of the particle-size domain and the representation of spatial information, either by directly parametrising aggregation/breakage rates using CFD-resolved quantities or by incorporating local hydrodynamic data from CFD into the population dynamics. Among the available approaches, the sectional method is the most established and widely implemented formulation in CFD–PBM simulations of gas–solid and liquid–liquid systems. In this technique, the continuous particle-size domain is divided into

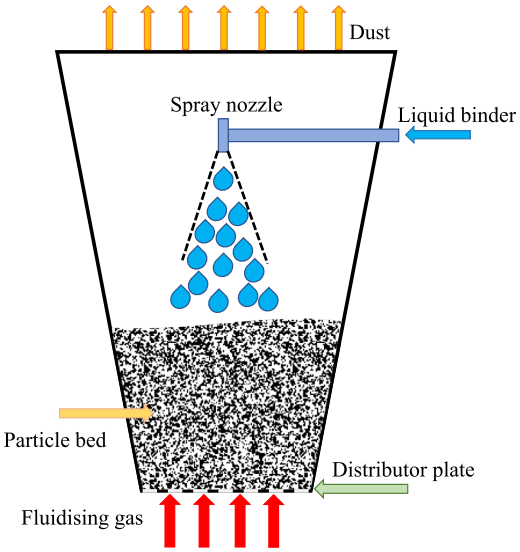

Fig. 1. Schematic representation of a top-spray fluidised bed granulator (SFBG), showing the fluidising-air inlet and distributor, particle bed, binder atomiser and spray zone, and the exhaust/dust outlet.

a finite number of size intervals ("sections or cells"), and the PBM is solved for the temporal evolution of the number or mass fractions within each interval. The fixed-pivot technique is considered one of the most robust implementations, as it ensures exact mass conservation during aggregation and breakage [27]. Discretised sectional formulations were initially proposed by Hounslow et al. [28], and subsequent studies have applied similar discretised PBMs within Eulerian–Eulerian CFD solvers [29], demonstrating their ability to represent coalescence and breakage phenomena across various regimes. Despite their conceptual simplicity, sectional methods have several limitations: accuracy depends strongly on the resolution of the size grid, and the computational cost increases rapidly with the number of sections because each CFD control volume must solve the corresponding set of PBE equations [19,30]. Furthermore, detailed balance may be violated for certain kernel forms in aggregation-dominant systems, potentially affecting long-term predictions of PSD [31].

To reduce the stiffness and dimensionality inherent in sectional PBMs, moment-based methods were introduced. The method of moments (MOM) [32], quadrature method of moments (QMOM) [33], and direct quadrature method of moments (DQMOM) [34], which approximate the PSD using a finite set of its moments rather than explicit size bins. This approach reduces the PBE to a smaller system of transport equations for the low-order moments of the distribution, thereby improving computational efficiency. Moment methods have been successfully integrated into CFD solvers for aggregation, breakage, and combined systems [35], enabling spatially resolved predictions of average granule size and variance with reduced cost. However, they rely on closure assumptions to reconstruct higher-order moments and may lose accuracy when simultaneous aggregation and breakage occur or when distributions are strongly multimodal [36]. Moreover, additional tools are required to estimate the PSD from the moments.

To overcome these issues, a finite-volume scheme (FVS) for the PBM has been utilised [37–39]. FVS discretisations are conservative by design, ensuring mass preservation, and offer robust numerical convergence on non-uniform grids, thereby remaining efficient and accurate for long-term simulations across a broad range of PSDs [40,41]. However, despite these numerical advantages, FVS has been applied under the assumption that SFBG is a homogeneous system. Liu et al. [9] introduced the concept of compartmentalisation in SFBG. In experimental observations, it was noted that particle wetting and drying are region-specific within the fluidised bed. Building on this concept, Kaur et al. [10] implemented a FVS discretisation within the compartmental framework, resulting in a two-compartment PBM. This method combines numerical robustness with a physically motivated representation of spatial heterogeneity in SFBG [42]. However, the model does not couple a two-compartment PBM with CFD, and compartmental exchange is modelled using empirical characteristic time ratios, defined as the aggregation time divided by the residence time. This limits their feasibility across operating conditions and restricts the degree to which spatial heterogeneity can be linked to measurable flow features. Briefly, it can be concluded from the above discussion that the existing coupled CFD–PBM models are computationally expensive for optimising the SFBG process, either because the CFD simulations are performed in a 3D domain or because the PBM is solved numerically using a large number of cells to capture the PSD with high accuracy [9,42].

In this work, our aim is to develop an efficient predictive reduced-order coupled CFD–PBM framework to optimise the sprayed fluidised bed granulator. In particular, CFD is used to track the exchange (fluxes) of particle properties between compartments using the Eulerian–Eulerian approach, replacing empirically tuned compartment parameters with physically derived quantities [10]. Once these fluxes are determined, they are incorporated into the PBMs formulated for each compartment. The resulting set of coupled PBMs is then solved using a two-moment preserving FVS, which ensures accurate tracking of the PSDs while maintaining consistency in the lower-order moments (e.g., total number and volume). This numerical framework enables stable and physically consistent

evolution of the PSDs under the combined effects of transport and particle interactions. Furthermore, the influence of aggregation kinetics on the evolution of the PSDs is systematically investigated by implementing and comparing different aggregation kernels. By analysing how various kernel formulations affect the shape and moments of the PSDs, the sensitivity of the system to underlying collision and coalescence mechanisms can be assessed, providing deeper insight into the governing particle dynamics.

The outline of the present work is structured as follows: the CFD setup and the governing equations, together with the discretised two-compartment PBM of FVS, are described in Section 2. The coupling CFD–PBM framework for the SFBG is presented in Section 3. Further Section 4 is used to describe the CFD simulations for the grid sensitivity analysis to analyse the dependency of the parameter on the cell count. The results obtained from the proposed framework are presented and validated against experiments in Section 5. Finally, the findings of this work are summarised and concluded in Section 6.

2. Mathematical model for SFBG

In this section, the coupled CFD–PBM framework for optimising the SFBG is described in detail. Section 2.1 provides an overview of computational modelling, outlining the fundamental governing equations utilised in the numerical investigation. These include Eq. (1) for the continuity equation, Eq. (2) for momentum conservation, and Eqs. (3)–(4) for the kinetic theory of granular flow, and Eqs. (5)–(6) for turbulence dynamics. The interaction between the gas and solid phases is defined by Eq. (7). Furthermore, to describe the particle-size evolution in the SFBG, a two-compartment PBM is used, which is discussed in Section 2.2. The FVS formulation used to solve these PBMs Eqs. (25) and (26) is given in detail in Eqs. (13) and (14). The aggregation and breakage kernels which govern the PSD are described in Section 2.3, followed by the parameter-estimation procedure in Section 2.4, which is used to determine the aggregation rate constant (β_0) and breakage rate coefficient (S_o).

2.1. CFD model

In the fluidised state, the bed exhibits fluid-like behaviour: particles move freely and mix vigorously, resulting in exchange between the compartments. Due to the dense nature of the fluidised bed and the strong interactions between the gas and solid phases, an Eulerian–Eulerian framework is used to model the conservation of mass and momentum, where both the phases are treated as interpenetrating continua [43]. The general form of the continuity equation for each phase is expressed as

$$\frac{\partial}{\partial t}(\alpha_q \rho_q) + \nabla \cdot (\alpha_q \rho_q \mathbf{u}_q) = 0 \tag{1}$$

which ensures mass conservation for both the gas and solid phases. The corresponding momentum conservation equation is given by

$$\frac{\partial}{\partial t}(\alpha_q \rho_q \mathbf{u}_q) + \nabla \cdot (\alpha_q \rho_q \mathbf{u}_q \mathbf{u}_q) = -\alpha_q \nabla p + \nabla \cdot \boldsymbol{\tau}_q + \alpha_q \rho_q \mathbf{g} + \sum_{p \neq q} \mathbf{K}_{pq}(\mathbf{u}_p - \mathbf{u}_q), \tag{2}$$

where α_q is the phase volume fraction, ρ_q and $\mathbf{u}_q$ are the density and velocity of phase q, and $\mathbf{K}_{pq}$ denotes the interphase momentum exchange term.

However, to represent fluidised bed dynamics accurately, the governing equations are closed using the kinetic theory of granular flow (KTGF) for modelling the solid-phase stress, granular temperature, and viscosity [43,44]. The solid pressure is defined as

$$p_s = \alpha_s \rho_s \Theta_s + 2(1 + e_{ss}) \rho_s \alpha_s^2 g_0 \Theta_s, \tag{3}$$

where Θ_s is the granular temperature, e_{ss} is the restitution coefficient and g_0 is the radial distribution function. The transport of granular temperature, which represents the fluctuating kinetic energy of the particles, is described by [44]

$$\frac{3}{2}\left[\frac{\partial(\alpha_s \rho_s \Theta_s)}{\partial t} + \nabla \cdot (\alpha_s \rho_s \mathbf{u}_s \Theta_s)\right] = \boldsymbol{\tau}_s : \nabla \mathbf{u}_s - \nabla \cdot (k_\Theta \nabla \Theta_s) - \gamma_\Theta, \tag{4}$$

where the terms on the right-hand side represent the production, diffusion, and dissipation of granular energy, respectively.

To capture the gas-phase turbulence and its interaction with the solids, a standard k–ε turbulence model is employed [8,45]. The transport equations for the turbulent kinetic energy (k) and its dissipation rate (ε) are given by

$$\frac{\partial(\rho k)}{\partial t} + \nabla \cdot (\rho \mathbf{u} k) = \nabla \cdot \left[\left(\mu + \frac{\mu_t}{\sigma_k}\right) \nabla k\right] + G_k - \rho \varepsilon, \tag{5}$$

and

$$\frac{\partial(\rho \varepsilon)}{\partial t} + \nabla \cdot (\rho \mathbf{u} \varepsilon) = \nabla \cdot \left[\left(\mu + \frac{\mu_t}{\sigma_\varepsilon}\right) \nabla \varepsilon\right] + C_{1\varepsilon} \frac{\varepsilon}{k} G_k - C_{2\varepsilon} \rho \frac{\varepsilon^2}{k}. \tag{6}$$

Here, $\mu_t = C_\mu \rho \frac{k^2}{\varepsilon}$ denotes the turbulent viscosity, while G_k represents the production of turbulent kinetic energy. The use of this model helps resolve turbulence generated by bubble formation and phase interactions in the bed.

The interaction forces between the gas and solid phases are accounted for using the Gidaspow drag correlation, which combines the Ergun equation for dense regions and the Wen–Yu model for dilute regions [43]. The drag coefficient is defined as

$$\mathbf{K}_{gs} = \begin{cases} 150\dfrac{(1-\varepsilon_g)\mu_g}{\varepsilon_g d_p^2} + 1.75\dfrac{\rho_g|\mathbf{u}_g - \mathbf{u}_s|}{d_p}, & \text{for } \varepsilon_g \le 0.8, \\ \dfrac{3}{4}C_D\dfrac{\varepsilon_g\varepsilon_s\rho_g|\mathbf{u}_g - \mathbf{u}_s|}{d_p}\varepsilon_s^{-2.65}, & \text{for } \varepsilon_g > 0.8, \end{cases} \tag{7}$$

where the particle Reynolds number and drag coefficient are expressed as

$$C_D = \frac{24}{Re_p}\left(1 + 0.15\, Re_p^{0.687}\right). \tag{8}$$

$$Re_p = \frac{\rho_g d_p \left|\mathbf{u}_g - \mathbf{u}_s\right|}{\mu_g}. \tag{9}$$

This correlation enables the model to account for spatial variation in void fraction and accurately predict interphase momentum exchange across different flow regimes.

2.2. Two-compartmental PBM

The mathematical formulation of the two-compartment PBM for the SFBG is presented by partitioning the system into two interacting regions: wetting compartment (WC) and drying compartment (DC), as shown in Fig. 2. Approximately 30% of the height of the bed (H_{bed}) is associated with the WC (H_{WC}), and 70% with the DC (H_{DC}) [9]. Using this prescribed compartment split, the solids-weighted compartment areas A_{WC} and A_{DC}, along with the inter-compartment exchange rates $R_{\text{WC}\to\text{DC}}$ and $R_{\text{DC}\to\text{WC}}$, are obtained from the fully developed CFD simulations and used as inputs to the PBM Eqs. (10) and (11). Aggregation is assumed to dominate in the WC because of active contact with the binder fluid and high surface stickiness. In contrast, breakage is assumed to predominate in the DC, where particles are comparatively drier and more fragile due to continuous interaction with the hot fluidising gas.

The compartment-specific assumption is adopted as a dominant-mechanism approximation rather than a complete exclusion of secondary mechanisms, such as limited breakage in the WC or residual aggregation in the DC. Earlier studies have shown that particle agglomeration is mainly associated with the wetting-active zone, where particle wetting and liquid-bridge formation occur; however, the size of this zone depends on the operating conditions rather than being universally fixed [46,47]. The wetting-active zone has been shown to occupy approximately 14%–30% of the bed depending on operating conditions [46,47], while Liu et al. [9] adopted a 30% WC/70% DC split in their TCPBM formulation. Following the two-compartment PBM formulation of Liu et al. [9], aggregation is retained in the WC and breakage in the DC to provide a physically interpretable reduced-order model while limiting the number of additional compartment-specific kernels and parameters. The predicted PSD may be sensitive to the prescribed WC/DC split, since changing the compartment definition would also affect the CFD-derived compartment areas, exchange rates, and effective particle residence in the aggregation- and breakage-dominant regions. The framework is expected to be most applicable when the WC and DC remain distinguishable, the prescribed split represents the dominant process zones, and the CFD-derived compartment areas and exchange rates capture the main solids holdup and circulation between compartments. A fully dynamic compartmentalisation, in which the WC/DC boundary evolves with process time, local binder saturation, moisture content, or hydrodynamic fields, is not considered in the present study.

Mathematically, a two-compartment PBM is utilised by applying the one-dimensional aggregation and breakage equations to both compartments, often expressed as integro-partial differential equations given by

$$\begin{aligned} \frac{\partial n_{\text{WC}}(x,t)}{\partial t} &= \frac{1}{2}\int_0^x \beta_{\text{WC}}(x-y,y,t)\, n_{\text{WC}}(x-y,t)\, n_{\text{WC}}(y,t)\, dy \\ &\quad - n_{\text{WC}}(x,t)\int_0^\infty \beta_{\text{WC}}(x,y,t)\, n_{\text{WC}}(y,t)\, dy + \frac{n_{\text{DC}}(x,t)\, R_{\text{DC}\to\text{WC}}}{A_{\text{DC}}} - \frac{n_{\text{WC}}(x,t)\, R_{\text{WC}\to\text{DC}}}{A_{\text{WC}}} \end{aligned} \tag{10}$$

$$\begin{aligned} \frac{\partial n_{\text{DC}}(x,t)}{\partial t} &= \int_x^\infty S_{\text{DC}}(y,t)\, \nu(y)\, b^*(x|y)\, n_{\text{DC}}(y,t)\, dy \\ &\quad - S_{\text{DC}}(x,t)\, n_{\text{DC}}(x,t)\int_0^\infty b^*(y|x)\, dy + \frac{n_{\text{WC}}(x,t)\, R_{\text{WC}\to\text{DC}}}{A_{\text{WC}}} - \frac{n_{\text{DC}}(x,t)\, R_{\text{DC}\to\text{WC}}}{A_{\text{DC}}} \end{aligned} \tag{11}$$

In Eqs. (10) and (11), $n_{\text{WC}}(x,t)$ and $n_{\text{DC}}(x,t)$ represent the number density functions with respect to the particle volume coordinate x at time t in the WC and DC, respectively. Here, x and y denote the particle volumes. Assuming spherical particles, the volume shape factor is $\pi/6$, and the equivalent particle diameter (d_p) is related to particle volume by $x = (\pi/6)d_p^3$. The terms involving $\beta(x,y)$ and $S(y)$ represent the aggregation kernel and breakage selection rate within each compartment, respectively. Moreover, in the event of a particle of volume y breaking into fragments of volume x, the functions $\nu(y)$ and $b^*(x|y)$ represent the number of fragments and daughter-fragment probability density function.

The finite volume discretisation of the two-compartment PBM, adapted from Kaur et al. [10], is described below (refer Eqs. (13) and (14)). The discretisation of Eqs. (10) and (11) is done under the assumption that all particles are concentrated at the centre of the cell (control volumes). For numerical implementation, the particle-size domain is divided into I size-classes indexed by

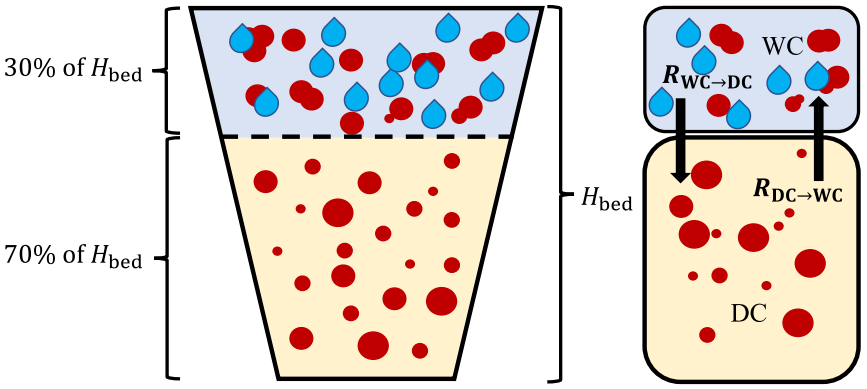

Fig. 2. Schematic representation of the two-compartment PBM for the SFBG. The bed is divided into the wetting compartment (WC) and drying compartment (DC), with compartment heights of $H_{WC} = 0.3\,H_{bed}$ and $H_{DC} = 0.7\,H_{bed}$, while the inter-compartment solids exchange is described by $R_{WC\to DC}$ and $R_{DC\to WC}$.

$i = 1, 2, 3, 4, \ldots, I$. Each size class i is bounded by $[x_{i-1/2}, x_{i+1/2}]$, with x_i being the middle point of the corresponding size interval. Here,

$$x_i = \frac{x_{i-1/2} + x_{i+1/2}}{2} \tag{12}$$

The final discretised form of the FVS for a two-compartment PBM (one-dimensional) is given by

$$\frac{dN_i^{WC}}{dt} = \frac{1}{2}\sum_{(j,k)\in\theta^i} \beta_{jk} N_j^{WC} N_k^{WC} \omega_{jk}^{b,WC} - N_i^{WC} \sum_{j=1}^{I} \beta_{ij} N_j^{WC} \omega_{ij}^{d,WC} + \frac{N_i^{DC} \times R}{A_{DC}} - \frac{N_i^{WC} \times R}{A_{WC}} \tag{13}$$

and

$$\frac{dN_i^{DC}}{dt} = \sum_{k=i}^{I} S_k N_k^{DC} \left[\int_{x_{k-1/2}}^{p_k^i} b(x, x_k)\, dx\right] \omega_k^{b,DC} - S_i N_i^{DC}\, \omega_i^{d,DC} + \frac{N_i^{WC} \times R}{A_{WC}} - \frac{N_i^{DC} \times R}{A_{DC}}. \tag{14}$$

Here, N_i^{WC} and N_i^{DC} denote the number of particles in the size class i in WC and DC, respectively. Under the assumption of quasi-steady exchange between the two-well mixed compartments, the transfer rates from WC to DC and from DC to WC are taken approximately equal, i.e. $R_{WC\to DC} \approx R_{DC\to WC} = R$ [9].

The set θ^i Eq. (15) identifies all size pairs (j, k) for which the combined size $(x_j + x_k)$ lies within the ith interval. Physically, this ensures that only those collisions capable of generating a particle belonging to size class i contribute to the aggregation gain term in the WC. In this sense, θ^i provides a volume-conserving mapping that assigns newly formed aggregates to the appropriate discretised size bin,

$$\theta^i = \left\{(j,k) \in I \times I \,:\, x_{i-1/2} < (x_j + x_k) \le x_{i+1/2}\right\}, \tag{15}$$

and includes a pair of indices of cells j and k, so that the sum $x_j + x_k$ is expected to fall in the ith cell. The weight factors $\omega_{j,k}^{b,WC}$, $\omega_{i,j}^{d,WC}$, $\omega_k^{b,DC}$, $\omega_i^{d,DC}$ are defined as

$$\omega_{j,k}^{b,WC} = \begin{cases} \frac{x_j + x_k}{2\,x_{p(i,j)} - (x_j + x_k)}, & x_j + x_k \le x_I \\ 0, & x_j + x_k > x_I, \end{cases} \tag{16}$$

$$\omega_{i,j}^{d,WC} = \begin{cases} \frac{x_{p(i,j)}}{2\,x_{p(i,j)} - (x_i + x_j)}, & x_i + x_j \le x_I \\ 0, & \text{otherwise}, \end{cases} \tag{17}$$

$$\omega_k^{b,DC} = \frac{x_k\left[\nu(x_k) - 1\right]}{\sum_{m=1}^{k}(x_k - x_m)\int_{x_{m-1/2}}^{p_k^m} b(x, x_k)\, dx}, \tag{18}$$

$$\omega_i^{d,DC} = \frac{\omega_i^{b,DC}}{x_i} \sum_{j=1}^{i} x_j \int_{x_{j-1/2}}^{p_i^j} b(x, x_j)\, dx, \tag{19}$$

where

$$p_k^i = \begin{cases} x_i, & i = k \\ x_{i+1/2}, & i \ne k. \end{cases} \tag{20}$$

Table 1
Aggregation kernels considered in the present study.

Kernel	Aggregation kernel, $\beta_{WC}(x, y)$	Source
Shear kernel	$\beta_0 \left(x^{1/3} + y^{1/3}\right)^3$	Smoluchowski [49]
Generalised shear kernel	$\beta_0 \left(x^{1/3} + y^{1/3}\right)^a$	Ding et al. [50] and Liu et al. [48]
Kapur kernel	$\beta_0 \dfrac{\left(x^{1/3} + y^{1/3}\right)^a}{\left(x^{1/3} y^{1/3}\right)^b}$	Kapur [51]
Brownian kernel	$\beta_0 \left(x^{1/3} + y^{1/3}\right)\left(x^{-1/3} + y^{-1/3}\right)$	Smoluchowski [49] and Skorych et al. [52]

For the generalised shear kernel, a controls the size dependence. In the present study, $a \in (0, 3]$, with $a = 3$ corresponding to the classical shear kernel. For the Kapur kernel, we consider $a = b$.

The discrete formulation, together with the weighting factors defined above Eqs. (16) to (19), ensures the conservation of the zeroth (number) and first (volume) moment in both compartments. The aggregation and breakage models and parameter estimation for the current study are presented in Sections 2.3 and 2.4.

2.3. Aggregation and breakage kernels

The aggregation and breakage kernels employed in the present study are discussed in this section. Aggregation predominates in the WC, whereas breakage is limited to the DC, consistent with the two-compartment PBM assumption. The Smoluchowski shear kernel is selected as the baseline aggregation model (refer Table 1). This kernel represents shear-induced particle collisions arising from velocity gradients in the surrounding binder and has been widely adopted in the PBM of fluidised beds and granulation systems [48]. In order to check the influence of the aggregation kernels, a sensitivity study has been done by considering different size-based kernels (generalised shear and kapur) and thermal diffusion-based kernel (Brownian kernel), and the effects of these kernels are studied and discussed in the results section (refer to Table 6).

Particle breakage in the DC is modelled using the size-based selection function $S(x)$ shown in Eq. (21), which controls the rate at which particles of volume x undergo breakage. Binary breakage is considered, meaning that a parent particle fragments into two daughter particles; this is represented in the finite-volume discretisation through Eq. (18), with $\nu = 2$. The daughter-size distribution is kept fixed, so that the sensitivity analysis remains focused on aggregation-kernel selection; therefore, the influence of alternative daughter-size distributions is not separately assessed. The daughter-fragment density function used in the model is given by Eq. (22).

$$S(x) = S_0\, x^{1/3}, \tag{21}$$

and

$$b^*(x, y) = \frac{1}{y}, \qquad 0 < x < y. \tag{22}$$

In all aggregation kernels, β_o (aggregation rate constant) and S_o (breakage selection constant) are treated as effective parameters that implicitly account for underlying process factors such as spray injection, binder transport, and drying.

2.4. Parameter estimation

The constants β_o, S_o, and a (aggregation kernel exponent) are estimated to optimise the CFD–PBM prediction to match experimental results. The size classes used in this study were kept consistent with the size classes of the experimental study of Liu et al. [9]. A total of 4 experiments (refer Table 5) were considered, and the parameters were estimated by minimising the cost function, the sum of squared errors (SSE) given by

$$\mathrm{SSE}(\beta_0, S_0, a) = \sum_{i=1}^{I} \left[\phi_i^{\mathrm{exp}} - \phi_i^{\mathrm{sim}}(\beta_0, S_0, a)\right]^2, \tag{23}$$

$$\phi_i^{\mathrm{sim}} = \frac{x_i N_i}{\sum_{j=1}^{I} x_j N_j} \tag{24}$$

where I denotes the total number of size classes, ϕ_i^{exp} and ϕ_i^{sim} represent the experimental and predicted normalised volume-based size fractions respectively, evaluated at size class i. The ϕ_i^{sim} is obtained by normalising the two-compartmental PBM predicted total particle volume, represented by each size class i (refer Eq. (24)), where x_i represents the particle-volume coordinate of size class i, and N_i denotes the corresponding PBM-predicted number of particles.

The minimisation carried out here follows a two-stage optimisation strategy: initially, a global search using the `Differential Evolution` [53] algorithm is employed to identify the region in the parameter space, followed by a local refinement using the `L-BFGS-B` (Limited-memory Broyden–Fletcher–Goldfarb–Shanno with Box constraints) [54] to obtain the final optimal parameter set.

Table 2
Values of parameters extracted from the 2D CFD simulation for PBM coupling.

Parameter	Value
Wetting compartment area, A_{WC} (m^2)	2.026×10^{-3}
Drying compartment area, A_{DC} (m^2)	2.792×10^{-3}
Particle-exchange rate in drying compartment, $R_{DC\to WC}$ (m/s)	3.98×10^{-4}
Particle-exchange rate in wetting compartment, $R_{WC\to DC}$ (m/s)	3.92×10^{-4}
Overall rate, R (m/s)	3.95×10^{-4}

Table 3
Values of parameters used in the CFD simulation.

Property	Value
Gas density (kg/m^3)	1.225
Gas viscosity ($kg/m\,s^{-1}$)	1.7894×10^{-5}
Solid particle density (kg/m^3)	450
Superficial inlet velocity (m/s)	0.086
Particle diameter (μm)	164
Initial solid packing	0.5273
Initial bed height (cm)	8.75
Restitution coefficient	0.9
Time step (s)	1×10^{-3}
Convergence criteria	1×10^{-6}
Operating pressure (Pa)	101 325
Maximum iterations per step	200

3. Coupled CFD–PBM framework

The coupling of the CFD and PBM is established externally. Once the CFD solution reaches a pseudo-steady state, the simulation is continued up to $t = 10$ s, and the time-averaged CFD fields are extracted. These averaged-quantities are then used to compute the parameters A_{WC}, A_{DC}, $R_{WC\to DC}$, and $R_{DC\to WC}$ using Eqs. (25) to (28) to calculate the effective area and the exchange rates of the solid in WC and DC, respectively.

$$A_{WC} = \sum_{a_c \in WC} \overline{\alpha_{s,c}}\, a_c, \tag{25}$$

$$A_{DC} = \sum_{a_c \in DC} \overline{\alpha_{s,c}}\, a_c, \tag{26}$$

$$R_{DC\to WC} = \sum_{\ell_c \in interface} \overline{\alpha_{s,c}}\, \ell_c\, \overline{v_c^{+}}, \tag{27}$$

and

$$R_{WC\to DC} = \sum_{\ell_c \in interface} \overline{\alpha_{s,c}}\, \ell_c\, \overline{v_c^{-}}. \tag{28}$$

Here, a_c denotes the area of the computational cell c in the 2D domain, and $\overline{\alpha_{s,c}}$ is the corresponding time-averaged solid volume fraction. The quantities A_{WC} and A_{DC} therefore represent the compartment areas weighted by the local solids content, and are used in the normalisation of the PBM source terms. In Eqs. (27) and (28), ℓ_c is the line length of the interface segment associated with cell c, $\overline{v_c^{+}}$ and $\overline{v_c^{-}}$ are the vertical components of the average solid-phase vertical velocity directed from DC to WC and from WC to DC, respectively, and the summation is carried out over all interface cells, between WC and DC.

The directional exchange rates $R_{DC\to WC}$ and $R_{WC\to DC}$ differ by only about 1.5% (refer Table 2). Therefore, they are reasonably approximated by a single overall circulation rate, R, in Eqs. (13) and (14). The numerical values of A_{WC}, A_{DC} and R extracted from the CFD simulation are summarised in Table 2. The CFD–PBM coupling framework leads to post-processing of the CFD outputs, finite-volume discretisation of the PBM, and the parametric optimisation was developed using `Python 3.13`.

4. Grid sensitivity analysis

CFD simulations of the fluidised bed granulator were carried out in `ANSYS Fluent`, where the governing equations were solved using the finite-volume method within an Eulerian–Eulerian framework. The 2D geometry of the SFBG was generated in `SpaceClaim` software, whereas the meshing of the computational domain was generated in `ANSYS Fluent`. The computational domain is shown in Fig. 3. In the numerical simulation, the standard $\kappa-\epsilon$ model was employed to simulate turbulence in the fluidised-bed granulator, as described in Section 2.1. The computational domain was discretised using a structured, quad-dominant mesh. The boundary conditions consist of a velocity inlet with a porous distributor at the base, a pressure outlet at the top, and standard wall boundaries for the sides. No-slip wall conditions at both the air and solid interfaces, implying that the velocity component

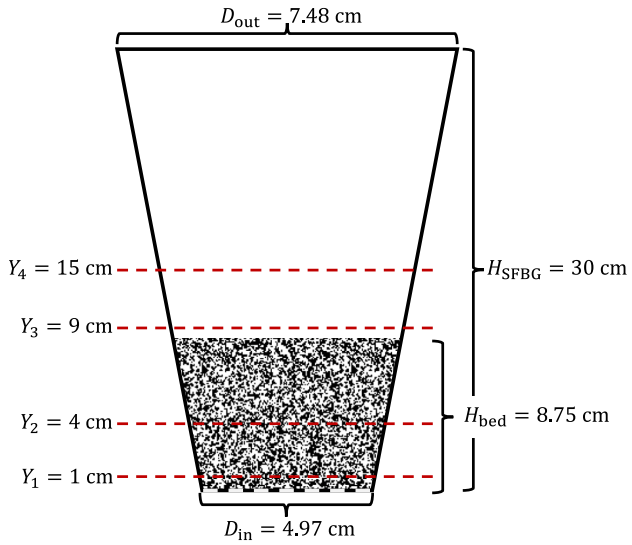

Fig. 3. Computational geometry of SFBG, showing the key dimensions (H_{SFBG}, H_{bed}, D_{in}, D_{out}) and the horizontal sampling lines (Y_1–Y_4) used to extract lateral hydrodynamic profiles within the bed. The boundary conditions were specified as a bottom-velocity inlet, a top-pressure outlet, and no-slip side walls.

Table 4
Mesh sensitivity analysis based on pressure drop and H_{bed} at $t = 4$ s.

Mesh	Cell width	Total cells	ΔP (Pa)	Bed height (m)	% diff. in ΔP	% diff. in bed height
Coarse	$10d_p$	5940	195.499	0.148976	0.2373%	1.6147%
Medium	$8d_p$	9316	195.964	0.151421	0.7926%	1.2078%
Fine	$7d_p$	12 246	194.423	0.149614	–	–

normal to the wall is zero. Pressure–velocity coupling was handled through the Phase-Coupled SIMPLE algorithm, while First-Order Upwind discretisation was applied to ensure numerical robustness and stability. A transient formulation with First-Order Implicit time-stepping was employed to accurately capture the dynamic behaviour of the fluidised bed. The convergence criteria were set to 1×10^{-6}, and the simulation was run until a quasi-steady state was reached ($t \sim 6$ s), after which time-averaging was performed over the next 4 s interval, i.e., from $t = 6$ to 10 s. A time-step of 1×10^{-3} s and 200 iterations per step were used throughout the computation. The material properties, operating conditions, and numerical parameters used in the CFD simulations are summarised in Table 3.

The numerical simulations were carried out on a workstation equipped with a 13th Gen Intel(R) Core(TM) i9-13900 processor (24 cores, 32 threads) and 64 GB of RAM, with `ANSYS Fluent` run in parallel on 16 CPU cores. Relatively long computational times, approximately 8 to 12 h, were required to complete a full CFD simulation up to $t = 10$ s. The use of a 2D simulation was primarily motivated by computational efficiency. For comparison within gas–solid fluidised bed simulations, Shi et al. [55] reported that for 20 s of physical process time, 3D simulation required approximately 2 weeks, whereas the 2D simulation took only 2–3 days. In the present study, a grid sensitivity analysis was conducted to assess the effect of mesh resolution on key hydrodynamic parameters. For the grid-sensitivity analysis, the 2D simulation results obtained using the superficial inlet velocity of 0.086 m s^{-1} were compared at $t = 4$ s. In the numerical simulation, two key parameters, the bed pressure drop (ΔP) and H_{bed}, were used in the grid-dependence test. Table 4 illustrates the grid sensitivity test for the SFBG. Temporal stability was ensured by maintaining the Courant number below 0.5 at all mesh levels. The investigation was performed for three distinct cell widths: $10d_p$, $8d_p$, and $7d_p$, which correspond to the coarse (5940 cells), medium (9316 cells), and fine (12 246 cells) mesh configurations, respectively. All the meshes used uniform grid spacing, with quad-dominant cells. The relative difference between the meshes was reduced from 1.6147% to 1.2078% for the H_{bed} and from 0.2373% to 0.7926% for the ΔP. Furthermore, the grid sensitivity test is illustrated graphically in Fig. 4. The variation in ΔP between the coarse and medium meshes, as well as between the medium and fine meshes, is observed to be less than 1%. Additionally, the H_{bed} shows a discrepancy of less than 2% across all mesh configurations. Consequently, the parameters used in this study were derived from the fine-mesh configuration ($7d_p$).

5. Results and discussions

In this section, we analyse the findings of the coupling framework, focusing on the CFD-based results and the two-compartment PBM-based predictions within the SFBG process. Hydrodynamic analyses examine CFD results with respect to variations in ΔP,

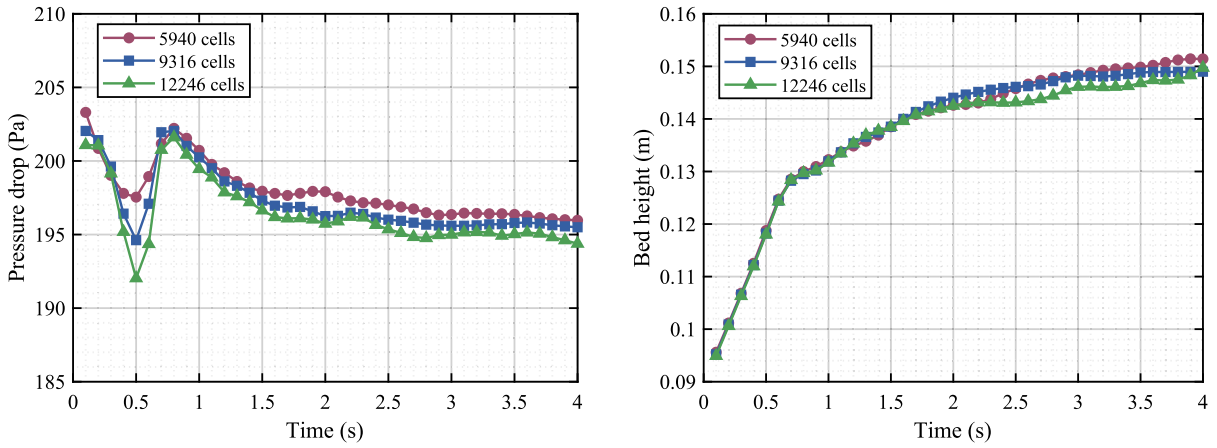

(a) Pressure drop (b) Bed height

Fig. 4. Variation of pressure drop (ΔP) and bed height (H_{bed}) of the SFBG with different cell counts for the grid-sensitivity test. The left figure illustrates the ΔP, while the right figure displays the corresponding H_{bed}.

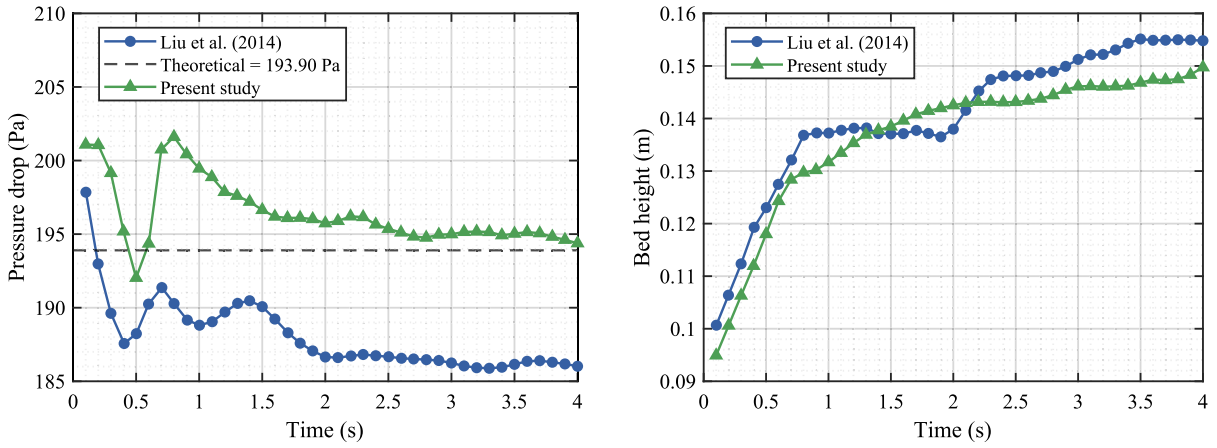

(a) Pressure drop (b) Bed height

Fig. 5. Comparison of the variation in pressure drop and bed height of the SFBG from the current numerical simulation with experimental results from the literature [9] and theoretical values. (For interpretation of the references to colour in this figure legend, the reader is referred to the web version of this article.)

H_{bed} (refer to Section 5.1), the temporal variation of the solid volume fraction (α_s) (refer to Section 5.2), and the significance of time-averaged solid volume fraction distribution ($\overline{\alpha_s}$) along the lateral distance of the SFBG chamber (refer to Section 5.3). These CFD results provide insight into the behaviour of the 2D SFBG simulation and form the basis for the subsequent PBM analysis, which highlights the evolution of the distribution of particles within fluidised bed, as discussed in Section 5.4. Additionally, Section 5.5 illustrates the impact of different aggregation kernels on the evolution of PSD within the SFBG. The coupled model predictions are compared with experimental data reported in the literature [9], and a comparative assessment of the 2D and 3D CFD model results is also presented.

5.1. Variation of hydrodynamic parameters

ΔP and H_{bed} are essential parameters in a fluidised bed granulation, as they provide direct insights into the hydrodynamic state, commonly referred to as fluidisation quality. These parameters are crucial for determining the endpoint of the granulation process and significantly influence the physical characteristics of the final granules. In the past, several researchers [9,56–58] have investigated these parameters in the analysis of fluidised bed granulation. The effectiveness of the present numerical simulations is compared against the model of Liu et al. [9], as illustrated in Fig. 5. The 3D model was employed for both the CFD analysis and the experimental study reported in Ref. [9]. The theoretical pressure drop (ΔP_{th}) value is estimated to be approximately 193.90 Pa, as calculated using Eq. (29) (Eq. 15 from Ref. [9]), as shown in the black dashed line in the Fig. 5(a). In this relation, the ΔP_{th} is

obtained from the balance between the upward pressure force exerted by the gas and the weight of the particle bed at minimum fluidisation:

$$\Delta P_{\mathrm{th}} = (\rho_s - \rho_g)(1 - \varepsilon_{\mathrm{mf}})gH_{\mathrm{mf}} + \varepsilon_{\mathrm{mf}}\rho_g g H_{\mathrm{mf}} + \rho_g g\left(H_{\mathrm{SFBG}} - H_{\mathrm{mf}}\right) \tag{29}$$

where ρ_s and ρ_g are the solid and gas densities, respectively, $\varepsilon_{\mathrm{mf}}$ is the bed voidage at minimum fluidisation, H_{mf} is the bed height at minimum fluidisation, and H_{SFBG} is the total height of the granulator. The values H_{mf} = 12.7 cm and $\varepsilon_{\mathrm{mf}}$ = 0.6588 are taken from Ref. [9]. This ΔP_{th} value is considered as a reference for incipient fluidisation; in the simulations, ΔP may vary during the start-up transient before settling into a quasi-steady state. In the context of the literature [9] regarding 3D numerical modelling, ΔP were determined to be approximately 197.84 Pa at 0.1 s and 186.03 Pa at 4 s, as shown in the solid blue line of Fig. 5(a). This indicates a reduction in the reported ΔP between the initial transient and later times, noting that ΔP within the fluidised beds exhibits time-dependent variations, and the observed trend depends on the averaging window and the definition of ΔP within the domain.

In contrast, the current 2D CFD analysis reveals a ΔP of 202.34 Pa at the initial time of 0.1 s, which decreases to 194.42 Pa at 4 s, as shown by the solid green line in Fig. 5(a). This trend indicates a gradual reduction in ΔP as the system evolves towards a quasi-steady regime within the simulated time window. The variation in ΔP between the 2D and 3D cases is also illustrated in Fig. 5(a). This comparison indicates that the pressure variation in the present study converges towards ΔP_{th} in the 2D case, whereas it diverges in the 3D case [9]. The calculated ΔP from the 2D model exhibits a deviation of approximately 0.52 Pa from the ΔP_{th}, while the literature-based 3D model shows a discrepancy of approximately 7.87 Pa. This comparison is used as a global hydrodynamic consistency check based on the bed-weight ΔP estimate. Since ΔP and H_{bed} are global quantities, they do not by themselves fully characterise local hydrodynamic features such as bubble dynamics, solids circulation, wall effects, or compartmental exchange rates. The percentage discrepancy between the 2D and 3D models was evaluated to quantify their difference in ΔP prediction for the SFBG. At 0.1 s and 4 s, the observed percentage differences were 2.22% and 4.32%, respectively. These results suggest that the 2D model captures the ΔP behaviour reasonably well while also offering reduced computational cost.

Fig. 5(b) illustrates the variation in H_{bed} observed in the current 2D CFD results compared to the literature-based [9] 3D model across various time scales. The results from the 2D and 3D models are illustrated by the green and blue solid lines, respectively. In the 3D model, H_{bed} is approximately 0.10 m at the initial time scale of 0.1 s, reaching nearly 0.15 m at 4 s. Conversely, for the 2D model, the initial H_{bed} is around 0.095 m at 0.1 s and increases to approximately 0.1496 m by the steady state at 4 s. These findings highlight differences in the dynamics of H_{bed} in the SFBG between the two modelling approaches. The percentage difference in H_{bed} between the current 2D and 3D models is assessed. Initially, a discrepancy of 5.1% is observed between the two models. This difference decreased over time, with the percentage difference reduced to 2.66%. Overall, Fig. 5 suggests that 2D and 3D models yield similar values for both ΔP and H_{bed} by the end of the simulation time window (4 s).

5.2. Variation of solid volume fraction

This section discusses the hydrodynamic behaviour from the 2D CFD simulations of the fluidisation process, focusing on instantaneous α_s and its comparison to the 3D literature model [9]. The instantaneous α_s represents the local volume fraction occupied by solids at each time and position. The 2D numerical simulation is conducted for a time span of 10 s, and the system approaches a statistically steady regime within this time.

A similar time span is considered in the literature model for 3D geometry [9]. To demonstrate the behaviour of the fluidised bed, Fig. 6 presents the visual contour plot of the instantaneous α_s derived from CFD simulations of the 2D SFBG over various time intervals. In this visualisation, the red colour corresponds to the peak α_s, while the blue colour indicates the minimum α_s, which is zero. During the initial moments of the simulation time around 0.1 s, the bed is packed up to H_0 = 8.75 cm, and the solids are nearly uniform in the dense region. Similar phenomena are also captured by the literature model [9] (refer to Fig. 4). A close correlation is observed between the 2D and 3D models at the onset of the fluidised simulation. Initially, both the 2D and 3D models demonstrate similar behaviour and H_{bed}. However, significant difference emerge over longer timescales, revealing the divergence between the two modelling approaches. At t = 0.4 s, the 2D and 3D models show a qualitatively similar α_s pattern, but differ in the local magnitude and spatial distribution of solids concentration. This is mainly due to the absence of out-of-plane motion of solids and three-dimensional bubble structures in the 2D formulation. According to fluidised flow physics, the superficial gas velocity represents the inlet gas velocity through a packed bed in the SFBG, which causes a disturbance in the solid bed voidage, leading to the fluctuations in the H_{bed}. With increasing time, the α_s field clearly illustrates the dynamic evolution of the gas–solid flow structure inside the fluidised bed. At very early times (t ∼ 0.1–0.8 s), the bed remains close to its initially packed condition, with predominantly high α_s (red) throughout the lower region and only small blue voids forming as the injected gas begins to overcome particle weight and initiate fluidisation.

As time progresses (t ∼ 1–3 s), these small voids grow and coalesce into larger bubbles, producing elongated blue channels that rise through the bed while dense red regions are displaced upward and laterally. This stage is characterised by bubbling behaviour and spatial heterogeneity, as particles are carried upward in bubble wakes and descend along the sides, describing a core-annulus type solid circulation pattern. At later times (t ∼ 4–9 s), the bed gradually transitions from the bubbling stage towards a statistically steady regime, which becomes apparent from approximately t ∼ 6 s onward. In this regime, large bubbles break into smaller, more uniformly distributed voids and α_s becomes more spatially distributed throughout the bed. This temporal transition from a dense-packed structure to bubbling and finally to a statistically steady regime reflects the influence of gas-particle drag and bubble-induced solids motion, which collectively establish stable fluidisation within the bed.

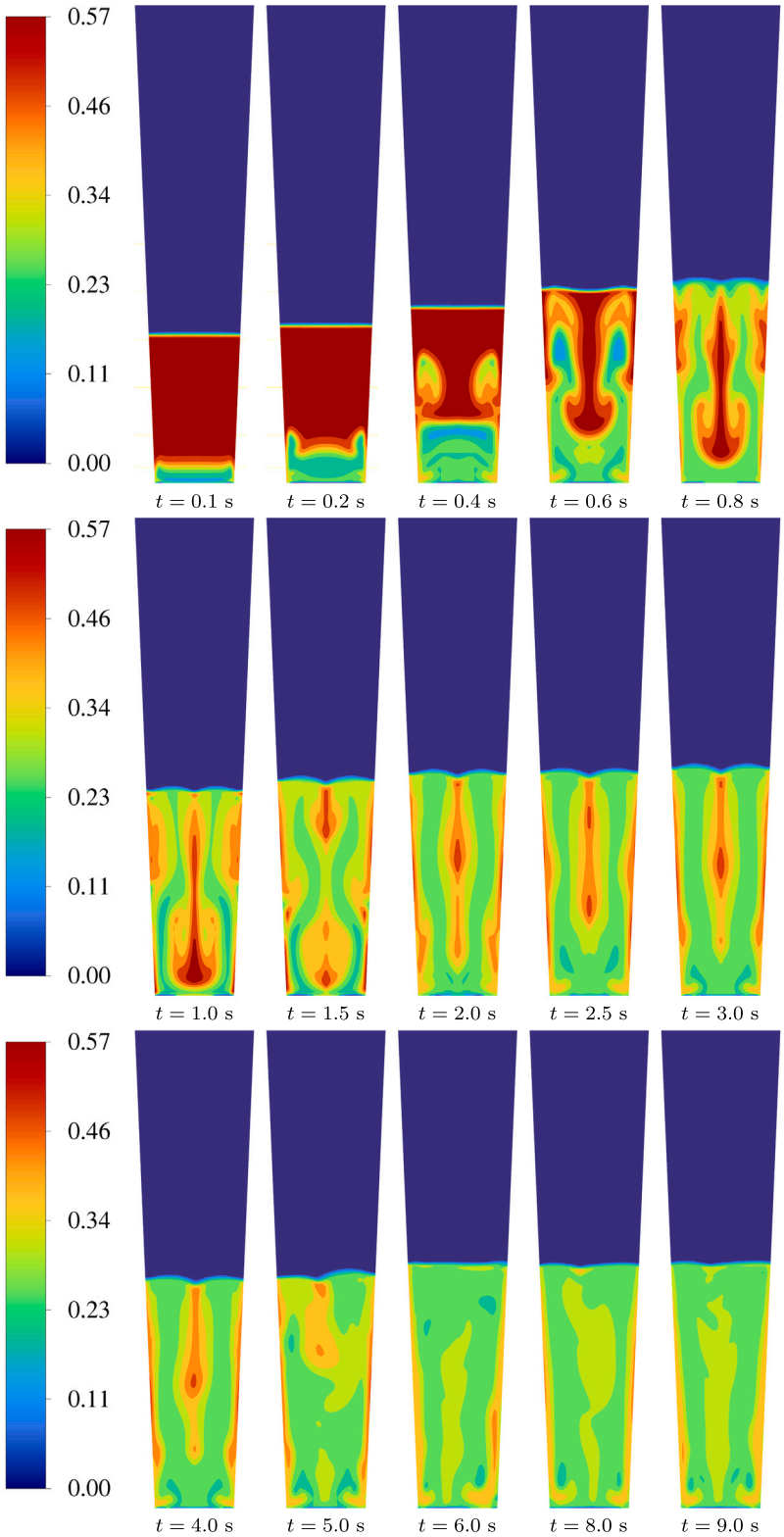

Fig. 6. Variation of instantaneous solid volume fraction (α_s) in the fluidised bed. The colour map illustrates the solid volume fraction, where red denotes regions of high particle concentration and blue represents voids filled with gas. (For interpretation of the references to colour in this figure legend, the reader is referred to the web version of this article.)

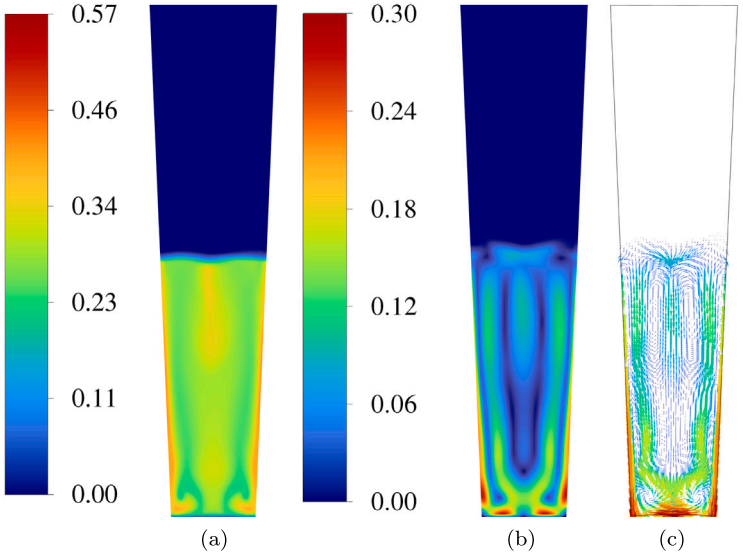

Fig. 7. Time-averaged CFD fields obtained over the interval t = 6–10 s: (a) time-averaged solid volume fraction $\overline{\alpha_s}$, (b) time-averaged solid velocity magnitude $\overline{U}$ [m s^{-1}], and (c) time-averaged solid velocity vector field illustrating the circulation pattern within the bed.

In this study, H_{bed} begins to stabilise at t = 6.0 s in the 2D case, and a similar time frame is also observed in the 3D case. Beyond this time, the bed exhibits a statistically steady fluidisation, with a slightly lower solid concentration near the wall, as observed in the 3D model.

The time-averaged solid volume fraction ($\overline{\alpha_s}$) defined in Eq. (30) is used to characterise the mean bed structure, since a gas–solid fluidised bed exhibits inherently unsteady behaviour due to solids circulation, resulting in rapid spatial and temporal fluctuations. The time-averaged α_s is defined as

$$\overline{\alpha_s}(\mathbf{X}) = \frac{1}{t_2 - t_1} \int_{t_1}^{t_2} \alpha_s(\mathbf{X}, t)\, dt, \tag{30}$$

where $\alpha_s(\mathbf{X}, t)$ denotes the instantaneous solid volume fraction at spatial location $\mathbf{X}$ within the flow domain and time t. Statistical sampling was performed over the interval t = 6–10 s after the flow reached a statistically steady regime. A single time step captures only transient bubble structures, whereas the time-averaged field offers the representative solids distribution within the bed.

The $\overline{\alpha_s}$ provides insight into the mean bed structures and solids transport within the region of the bed. The distribution of solids is denser in the lower regions and progressively dilutes towards the freeboard, as expected for bubbling fluidisation, where short-lived instantaneous bubbles are filtered out by time-averaging as shown in Fig. 7(a). This yields a characteristic, broad, wavy bed interface, typical of bubbling fluidisation regimes, where time-averaging eliminates sharp, instantaneous heterogeneities. In the middle panel, the movement of solids in the central and lower parts of the bed occurs at higher velocities, while the velocities near the walls in the upper regions are lower. This pattern aligns with bubble-driven transport seen in fluidised beds. The solid flow pattern within the bed resembles a core-annulus circulation, as illustrated in Fig. 7. In this situation, solid particles rise through the bed's central core, while descending along the walls. Fig. 7(b) illustrates the velocity magnitude of the solids. The relatively high values observed near the lower wall regions correspond to the downward particle motion along the walls, forming the descending branch of core-annulus circulation, which is also confirmed by the velocity vectors shown in Fig. 7(c). This motion facilitates continuous interaction between the dense and dilute phases within the system. The previously discussed concepts and the solid's behaviour are depicted in vector form, illustrating the velocity magnitude as shown in the right panel of Fig. 7.

5.3. Distribution of solid volume fraction

Fig. 8 shows the variation of solid volume fraction (α_s) between instantaneous and time-averaged profiles at different heights within H_{bed}, such as Y = 1 cm, 4 cm, 9 cm and 15 cm, along the lateral X-direction of the SFBG domain. These heights correspond to the horizontal sampling lines indicated in Fig. 3. The lateral distribution of α_s across the entire width of the bed at the final time step are presented. In this figure, the dashed line represents the instantaneous distribution at the final time step, while the solid line corresponds to the time-averaged profile obtained over the statistically stationary regime. At Y = 1 cm, the highest α_s is observed near the channel wall for both the instantaneous and time-averaged profiles, whereas the lowest values occur near the centre of the channel, as shown in Fig. 8(a). The instantaneous profile exhibits stronger oscillations than the time-averaged distribution due to transient bubble passage. This behaviour reflects the strong local fluctuations occurring near the distributor region. The superficial gas velocity represents the effective inlet gas velocity passing through a packed bed in an SFBG, leading to perturbations in the H_{bed}.

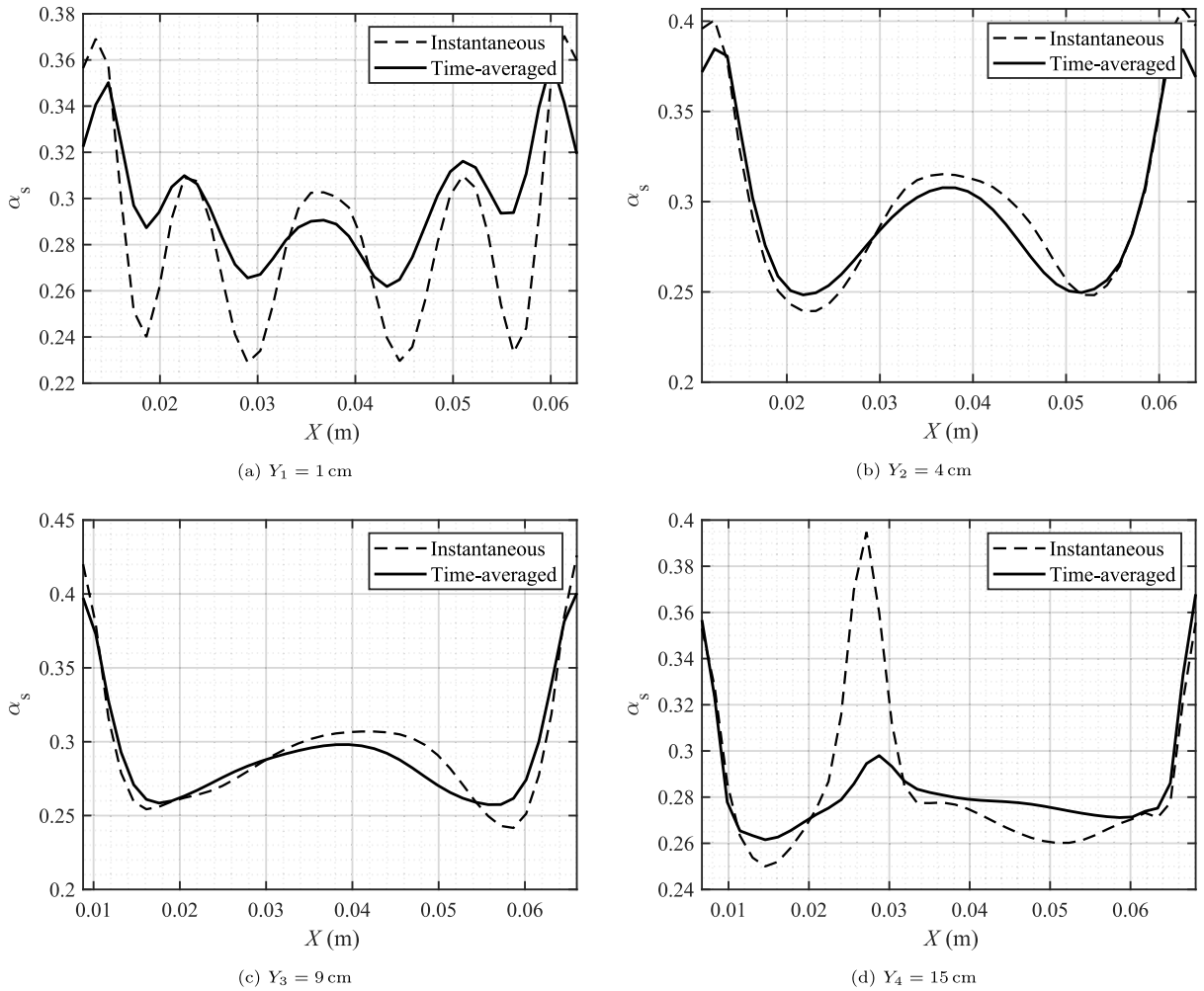

Fig. 8. Variation of the solid volume fraction (α_s) along the lateral X-direction at different bed heights (Y = 1, 4, 9, and 15 cm), corresponding to the horizontal sampling lines shown in Fig. 3. The dashed and solid lines represent the instantaneous and time-averaged values, respectively.

Therefore, the lateral variation of the instantaneous and time-averaged solids volume-fraction profiles is not perfectly uniform. At a slightly higher location, such as Y = 4 cm, the lateral variation of the α_s and $\overline{\alpha_s}$ profiles almost coincide, indicating that the solids distribution across the bed width becomes relatively uniform and symmetric, with weaker temporal fluctuations, as depicted in Fig. 8(b). A comparable behaviour is observed at Y = 9 cm, as illustrated in Fig. 8(c), where the instantaneous and time-averaged profiles remain very similar and exhibit a smooth lateral distribution. However, further upstream at Y = 15 cm, a distinct disparity emerges between the instantaneous and time-averaged solid volume fraction profiles, as depicted in Fig. 8(d). At this elevation, the instantaneous profile fails to capture the peak α_s near the wall, whereas the time-averaged profile does. This observation indicates that the instantaneous profile attains its maximum α_s at approximately $X \sim 0.03$ m, whereas the time-averaged profile attains its minimum α_s at the same spatial coordinate. This divergence underscores the importance of time averaging for accurately characterising the distributions of α_s in complex flow environments.

At significant heights, specifically at Y = 4 cm and Y = 9 cm, the profile of the α_s exhibits a pronounced smoothing effect and demonstrates a clear dependency on wall interactions. The distribution of α_s reveals an increase in solid concentration in proximity to the lateral boundaries, while the core region maintains a relatively lower α_s. This behaviour indicates a characteristic annular (wall-peaked) configuration typical of heterogeneous bubbling beds. The observed patterns of α_s are further illustrated in the contour plot presented in Fig. 6. The deviations between these two profiles reflect the inherently intermittent nature of bubbling fluidisation, in which the passage of bubbles and associated void-rich regions locally redistribute solids over short time scales. Although these instantaneous fluctuations can be significant, particularly in the lower and upper regions of the bed, the time-averaged profiles remain smooth and retain the same wall-peaked structure. This indicates that the observed lateral solids distribution is statistically stable and that the 2D CFD framework captures the mean hydrodynamic behaviour that drives the subsequent two-compartment PBM-based PSD analysis.

Table 5
Correspondence between the simulation cases and the experiments of Liu et al. [9], along with the PBM-predicted mean granule diameters in the WC and DC obtained in the present study.

Case	Liu et al. [9] experiment	$\bar{D}_{WC}$ (μm)	$\bar{D}_{DC}$ (μm)
Case 1	Experiment 2	639.93	559.72
Case 2	Experiment 3	425.32	391.70
Case 3	Experiment 4	493.03	486.60
Case 4	Experiment 5	417.73	393.48

5.4. Variation in particle size distribution

In this section, the PBMs for the WC and DC, given by Eqs. (10) and (11) are solved for the SFBG using a finite-volume approach. A detailed description of the finite-volume discretisation and the CFD–PBM coupling strategy is provided in Section 2.2. Fig. 9 presents the predicted normalised volume-based size fraction (ϕ) as a function of granule size in WC and DC for the four cases (cases 1–4), corresponding to selected experiments from Liu et al. [9] as summarised in Table 5. The compartment-wise granule size distributions provide insight into the characteristic size distribution within each compartment. The two-compartmental PBM predicted normalised volume-based size fraction (ϕ^{sim}) are shown in Fig. 10 and are compared with the experimental measurements (ϕ^{exp}) reported by Liu et al. [9] for model validation. Unlike the literature study, which implemented PBM using a discretised sectional approach, the current study uses a finite-volume formulation to solve PBM and a fully coupled CFD–PBM framework to capture hydrodynamics and granulation processes simultaneously.

In addition to the qualitative comparison of the PSD profiles, the granule size distributions were further characterised using the mean diameter ($\overline{D}$). This provides a quantitative measure of the representative size of the granule within the distribution and helps to assess the evolution of mean particle size. The mean diameter is calculated as

$$\bar{D} = \frac{\sum_{i=1}^{I} \phi_i \, d_i}{\sum_{i=1}^{I} \phi_i}, \tag{31}$$

where, ϕ_i denotes the normalised volume-based size fraction in the ith size class, d_i is the representative diameter (midpoint) of the ith size class, and I is the total number of size classes used to discretise the particle-size domain. The $\bar{D}$ is therefore a volume-weighted average diameter of the distribution. When evaluated for individual compartments, the corresponding notation $\overline{D}_{WC}$ and $\overline{D}_{DC}$ is used to denote the mean diameter in the WC and DC, respectively (refer Table 5).

The compartment-wise ϕ for all four cases are shown in Fig. 9 and are obtained from the baseline shear aggregation kernel. $\overline{D}$ is higher in the WC than in the DC in all cases (refer Table 5), indicating a greater contribution of larger granules in the WC. This is expected, as particles in the WC are wetted by the binder spray, promoting aggregation and resulting in larger granules. In contrast, the distributions within DC are generally characterised by peaks at smaller granule sizes, indicating an inclination towards fine particles in this compartment. This trend supports the assumption of breakage-dominant behaviour in the DC, where drying and particle collisions limit further granule growth. The extent of this compartmental difference, however, varies across all four cases. The difference between $\bar{D}_{WC}$ and $\bar{D}_{DC}$ within case 1 (refer Table 5) is approximately 14%, which indicates more aggregation domination (refer Fig. 9(a)). However, in cases 2, 3, and 4, the difference within the $\bar{D}_{WC}$ and $\bar{D}_{DC}$ is below 10%, stating that the compartmental segregation of granule size is relatively limited and hence indicating more balanced aggregation and breakage within the system. However, in case 3 shown in Fig. 9(c), a minimal difference between $\bar{D}_{WC}$ and $\bar{D}_{DC}$ is observed approximately 1.3%. This suggests that aggregation in WC and breakage in DC are less distinctly differentiated under these conditions.

Fig. 10 compares the predicted and experimental normalised volume-based size fractions (ϕ_i^{sim} and ϕ_i^{exp}, respectively) obtained using the baseline shear aggregation kernel. Overall, the 2D CFD-driven two-compartmental PBM reproduces the PSD shape and captures the approximate location of the dominant distribution peak across all four cases, indicating that the coupled framework provides a reasonable representation of granulation dynamics. The predicted distribution captures the shift in mass towards mid-sized granules and the overall decay towards larger sizes. The main deviation is observed in the peak region, where the framework tends to overpredict peak values in some comparisons, resulting in a slightly narrower distribution than the experimentally measured one. This may indicate that a multi-dimensional PBM is required to fully capture the system dynamics, including liquid distribution (which was neglected in the present study), as well as the PSD. Additionally, a generalised breakage kernel that allows the parent particle to fragment into more than two fragments may be required. Nevertheless, the simulations provide a consistent estimate of the dominant granule size range, serving as a predictive tool for optimising the SFBG and as a baseline for subsequent kernel sensitivity analysis.

5.4.1. Evolution of moments

The consistency of the two-compartmental PBM formulation is also assessed through the time evolution of the zeroth and first-order moments. In this study, the rth raw moments in the WC and DC at time t are defined as $M_r^{WC}(t) = \int_0^\infty x^r n_{WC}(x,t)\,dx$ and $M_r^{DC}(t) = \int_0^\infty x^r n_{DC}(x,t)\,dx$, respectively where $r = 0, 1$. The corresponding total-bed moment is calculated as $M_r^{tot}(t) = M_r^{WC}(t) + M_r^{DC}(t)$. The zeroth moment ($M_0^{tot}$) represents the total number of particles that decreases due to the aggregation mechanism in the WC and increases due to the breakage in the DC. However, the first moment (M_1^{tot}) represents the total volume of particles,

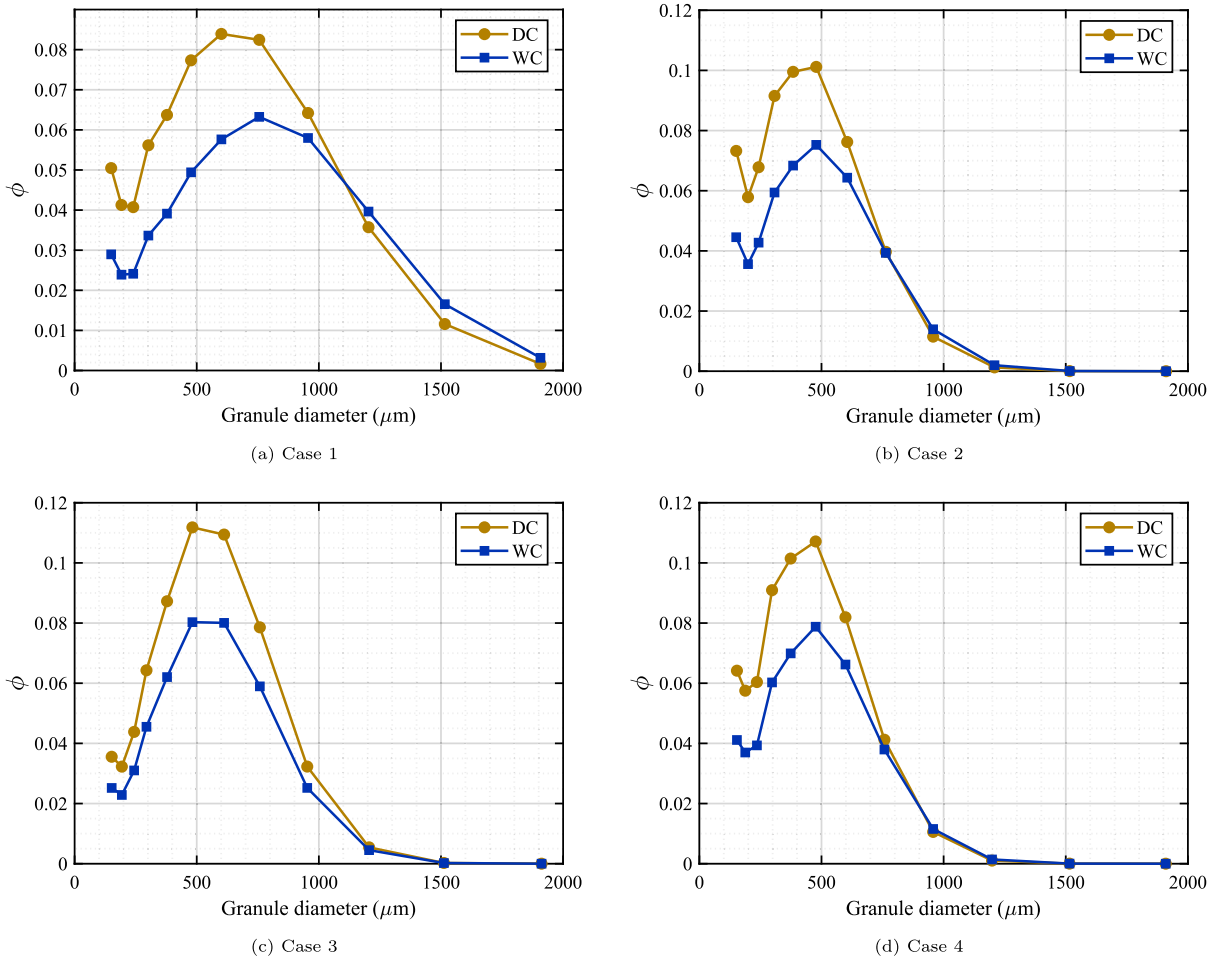

Fig. 9. Compartment-wise PBM-predicted normalised volume-based size fraction (ϕ) versus granule diameter in the wetting compartment (WC) and drying compartment (DC) for cases 1–4.

which remains approximately constant throughout the simulation. The qualitative behaviour of the M_0^{tot} and M_1^{tot} for all four cases is shown in Figs. 11 and 12, respectively. The normalised time is defined as t/t_{max}, where t_{max} is the final PBM simulation time. The zeroth moments shown in Fig. 11 are normalised with respect to the initial total particle number, $M_0^{\text{tot}}(0)$, while the first moments shown in Fig. 12 are normalised with respect to the initial total volume, $M_1^{\text{tot}}(0)$. It can be seen in Fig. 11(a), (b), (c), and (d) that the M_0^{DC} for all four cases decrease over time for the DC. However, the M_0^{WC} corresponding to the WC initially increases because more particles move from the DC to the WC than in the reverse direction. Thus, there is a sharper variation in the zeroth-order moment corresponding to the DC than the WC.

The M_1 in both WC and DC is shown in Fig. 12(a), (b), (c) and (d) for all four cases. Initially, all the particles are placed in DC, and solids are absent within WC. Once the simulation starts, solids are transferred within the WC and DC through the exchange term R in Eqs. (10) and (11) until a quasi-steady circulation is established. Later, the particulate volume in the WC remains unaltered over the time evolution, further supporting numerical consistency. This confirms that the FVS discretisation preserves the first moment, while allowing physically consistent changes in particle number. The same conservation behaviour was observed across all four simulation cases discussed in Section 5.4.

5.5. Effect of aggregation kernels on PSD

It is important to understand that the aggregation and breakage kernels play a significant role in capturing the PSD accurately in the SFBG process. To understand the influence of aggregation-kernel selection on predicted PSD, a comprehensive study is conducted. For our study, we have considered the binary breakage kernel and varied different aggregation kernels to understand the dynamics inside the SFBG. The accuracy is measured in terms of combining qualitative comparison of the volume fraction distributions (see Fig. 13) with quantitative error metrics, mean diameter ($\bar{D}$), and distribution relative widths (RW) reported in Tables 6 and 7.

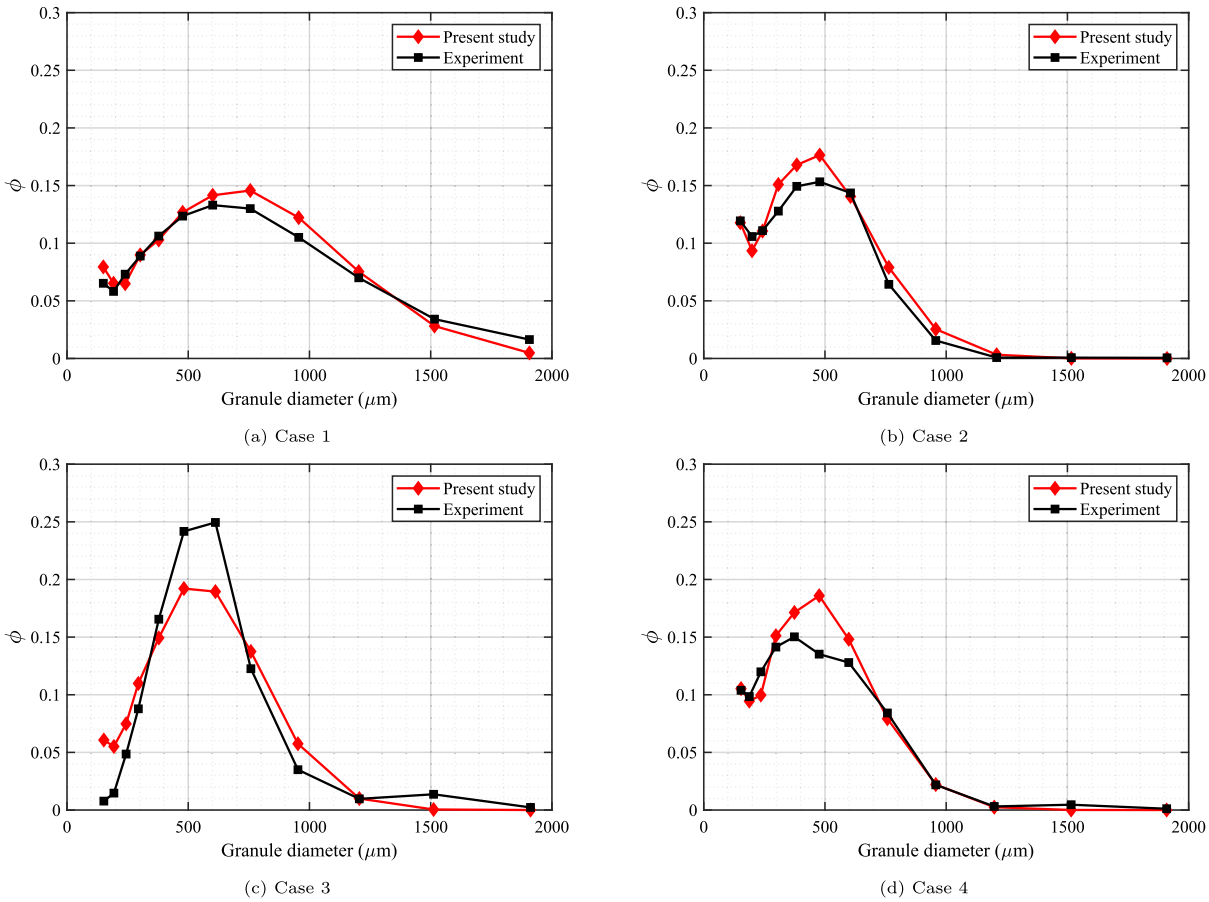

Fig. 10. Comparison of model-predicted and experimental normalised volume-based size fraction (ϕ) as a function of granule diameter for cases 1–4 using four aggregation kernels: shear, Brownian, generalised shear, and Kapur.
Source: The experimental data are taken from Liu et al. [9].

The $\bar{D}$ and RW of the granule size distribution are evaluated using the equations Eqs. (31) and (32)

$$RW = \frac{D_{90} - D_{10}}{\bar{D}}, \tag{32}$$

respectively. The quantities D_{10} and D_{90} in Eq. (32) correspond to the diameters at which 10% and 90% of the cumulative volume-based particle size distribution are undersized, respectively. The relative width RW provides a dimensionless measure of the distribution spread, normalised by the mean diameter.

The impact of aggregation kernel selection on the predicted PSD is initially evaluated qualitatively through the volume-fraction distributions shown in Fig. 13. Across all four cases, the coupled 2D CFD–PBM framework reproduces the overall shape of the experimental PSDs and captures the dominant granule-size range. However, slight differences are observed in the location of the peak magnitude and the decay in distributions closer to the coarse-particle side, depending on the chosen aggregation kernel. The generalised shear kernel is consistent throughout all cases, especially near the main peak, and exhibits a smoother decay with increasing particle size. The shear-kernel provides reasonable agreement with all 3 cases, but struggles to capture the peak in Case 3 (see Fig. 13). In contrast, the Kapur kernel exhibits sharp peaks and oscillatory behaviour on the coarse-particle side, particularly in Cases 2 and 4, indicating excessive sensitivity to size scaling. The Brownian kernel systematically underpredicts the population of larger granules, leading to visibly narrower distributions throughout all cases.

These qualitative observations are substantiated by quantitative metrics, including the SSE and $\overline{D}$ deviations, which are reported for each kernel and case as summarised in Table 6. The generalised shear kernel consistently yields lower SSE values across all four cases, as expected from Fig. 13, indicating improved agreement with the experimental PSDs. The shear kernel shows slight deviations, while the Kapur kernel produces significantly larger SSE values despite the presence of an additional fitting parameter. The Brownian kernel also exhibits higher errors, particularly when coarse-grain formation is prominent.

To further clarify kernel performance, the deviation in $\Delta\bar{D}$ is presented in Fig. 14. The generalised shear kernel demonstrates the most consistent deviations across all cases, whereas the Kapur kernel shows noticeable deviations across Cases 1, 2, and 3, with large

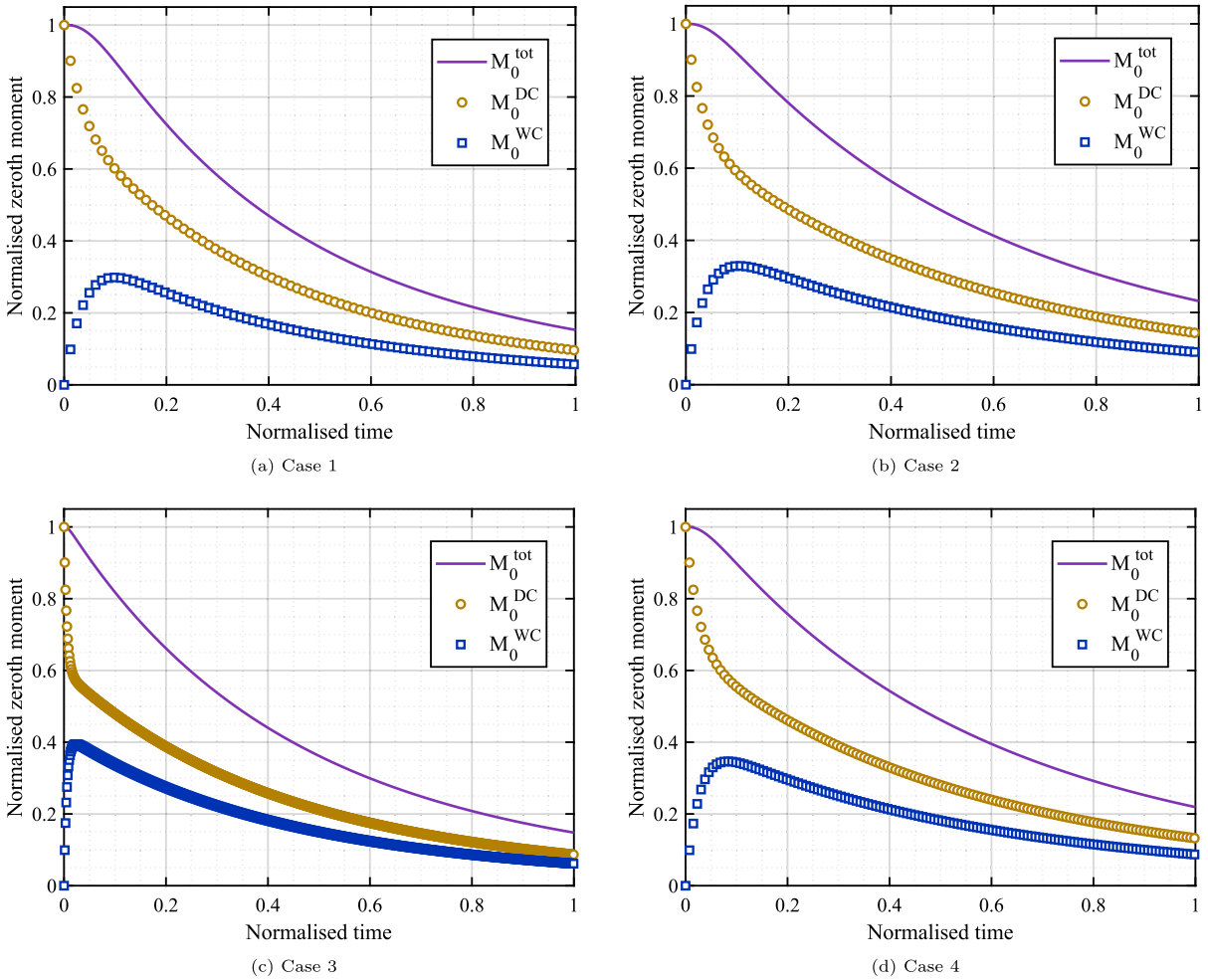

Fig. 11. Normalised evolution of the zeroth-moment. The figure shows the temporal evolution of the zeroth moment within the wetting compartment (WC, M_0^{WC}), drying compartment (DC, M_0^{DC}), and the total bed (M_0^{tot}) for cases 1–4.

Table 6
Fitted PBM parameters and mean diameter comparison for each kernel across all four cases.

Comparison	Kernel	β_0	S_0	a	SSE	$\bar{D}_*$ (μm)	$\bar{D}$ (μm)	$\Delta\bar{D}$ (%)
Case 1	Shear	402.729	1.04×10^{-6}	–	1.11×10^{-3}	607.947	593.241	−2.42
	Generalised shear	2267.126	4.95×10^{-8}	3.268	8.457×10^{-4}	607.947	594.122	−2.27
	Kapur	5447.985	90.926	4.537	1.206	607.947	570.699	−6.13
	Brownian	9.81×10^{-8}	1.74×10^{-6}	–	0.022	607.947	563.044	−7.39
Case 2	Shear	236.724	1.23×10^{-6}	–	0.927	393.066	405.760	+3.23
	Generalised shear	5601.353	7.59×10^{-7}	3.474	1.44×10^{-3}	393.066	405.271	+3.11
	Kapur	555.09	55.59	4.811	0.884	393.066	422.554	+7.50
	Brownian	2.32×10^{-8}	8.65×10^{-6}	–	0.017	393.066	407.121	+3.58
Case 3	Shear	37.326	1.06×10^{-6}	–	0.0128	537.263	489.305	−8.93
	Generalised shear	7.53×10^{-4}	1.05×10^{-7}	1.575	8.78×10^{-4}	537.263	510.518	−4.98
	Kapur	4988.807	51.451	4.708	1.411	537.263	509.008	−5.26
	Brownian	3.20×10^{-8}	3.58×10^{-6}	–	3.82×10^{-3}	537.263	491.112	−8.59
Case 4	Shear	167.20	5.23×10^{-7}	–	0.0039	402.707	403.632	+0.23
	Generalised shear	7999.99	1.92×10^{-7}	3.547	2.10×10^{-3}	402.707	406.055	+0.83
	Kapur	5199.90	91.79	4.521	1.195	402.707	454.362	+12.82
	Brownian	2.91×10^{-8}	4.04×10^{-6}	–	0.0173	402.707	384.670	−4.48

$\bar{D}_*$ are experimental values from Liu et al. [9]. (+) indicates overprediction, whereas (−) indicates underprediction relative to experiments.

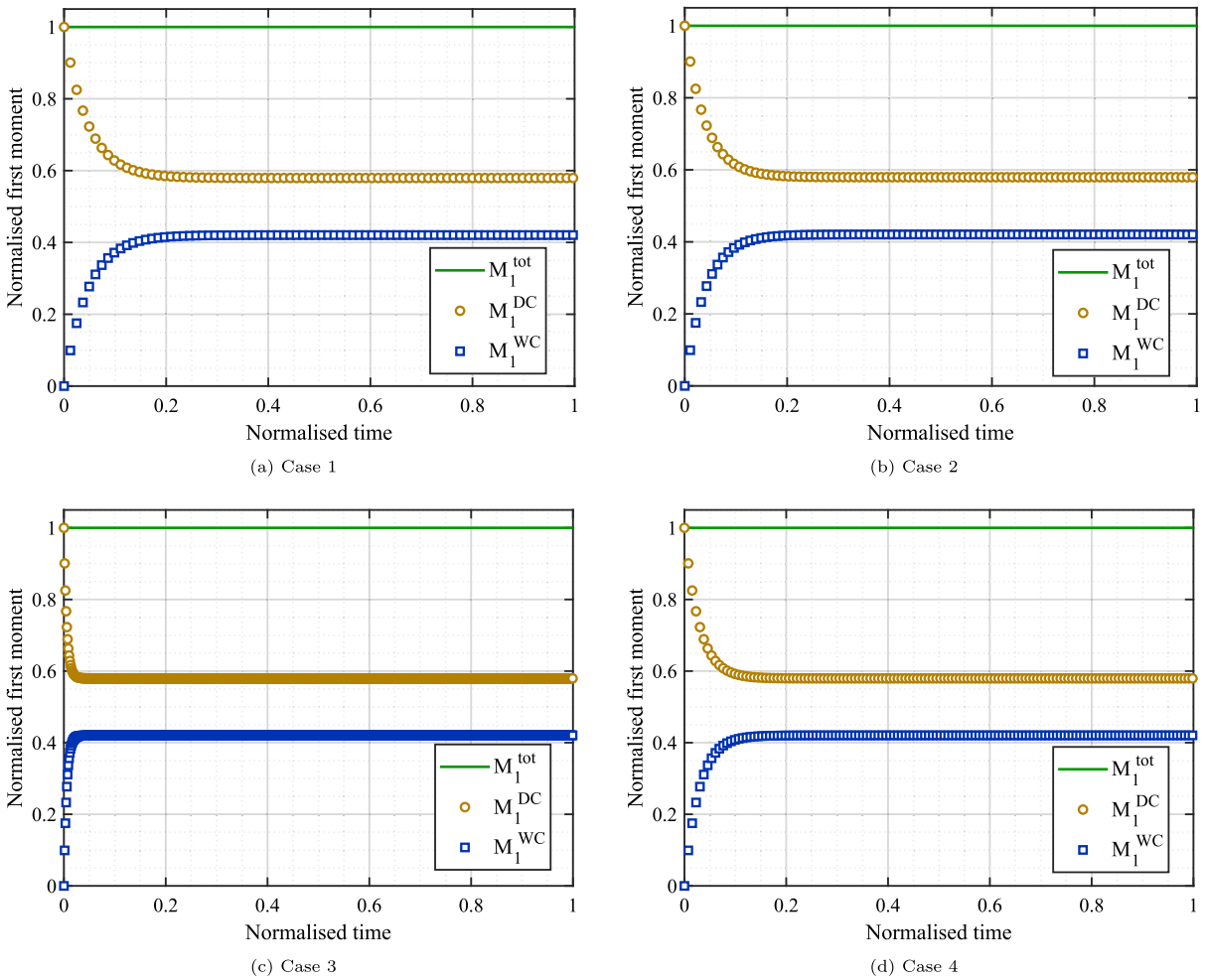

Fig. 12. Normalised evolution of the first moment. The figure shows the temporal evolution of the first moment within the wetting compartment (WC, M_1^{WC}), drying compartment (DC, M_1^{DC}), and the total bed (M_1^{tot}) for cases 1–4.

variation in Case 4. The Brownian kernel mostly underpredicts the $\Delta\bar{D}$, showing its tendency to subdue the formation of large-sized particles. These trends confirm that agreement in peak shape alone is insufficient, and that integral metrics such as $\Delta\bar{D}$ provide an essential complementary assessment.

Further differences in the particle distribution spread are assessed by the RW results presented in Table 7 and visualised in Fig. 15. The generalised shear kernel is in close agreement with the experiment in all four cases, whereas the shear kernel performs poorly in Case 3. In contrast, the Kapur and Brownian kernels exhibit large variations, either significantly narrowing or broadening the PSD, particularly in Case 3. The RW analysis reinforces the conclusion that kernels with an appropriate size-dependent collision scale better predicts both the peak magnitude and the spread of the PSD.

The fitted exponent a provides further insight into the robustness of the generalised shear kernel. In this kernel, a controls the dependence of the aggregation frequency on the collisional length scale $(x^{1/3} + y^{1/3})$. In Cases 1, 2, and 4, the fitted values of a are closer to 3; hence, it somewhat preserves the classical shear-type size dependence, where larger particles have greater weight in the process. Therefore, the improved performance of the generalised shear kernel was not obtained by abandoning the shear mechanism, but by allowing controlled flexibility in the particle-size dependence of aggregation. In Case 3, the lower value of $a \approx 1.575$ indicates a weaker size dependence, suggesting that aggregation was less dominated by larger particles and that smaller or intermediate particles relatively contributed more to the aggregation behaviour than predicted by the classical shear kernel. Overall, the combined analysis of the PSD profiles, fitted PBM parameters, $\Delta\bar{D}$, and ΔRW demonstrates that the generalised shear aggregation kernel provides the most consistent performance within the proposed 2D CFD–PBM framework. These results indicate that collision-driven aggregation mechanisms with balanced size dependence are more appropriate for modelling SFBG. In contrast, overly aggressive or diffusion-dominated kernels lead to systematic deviations in PSD shape and spread, as reflected by larger $\Delta\bar{D}$ and ΔRW values.

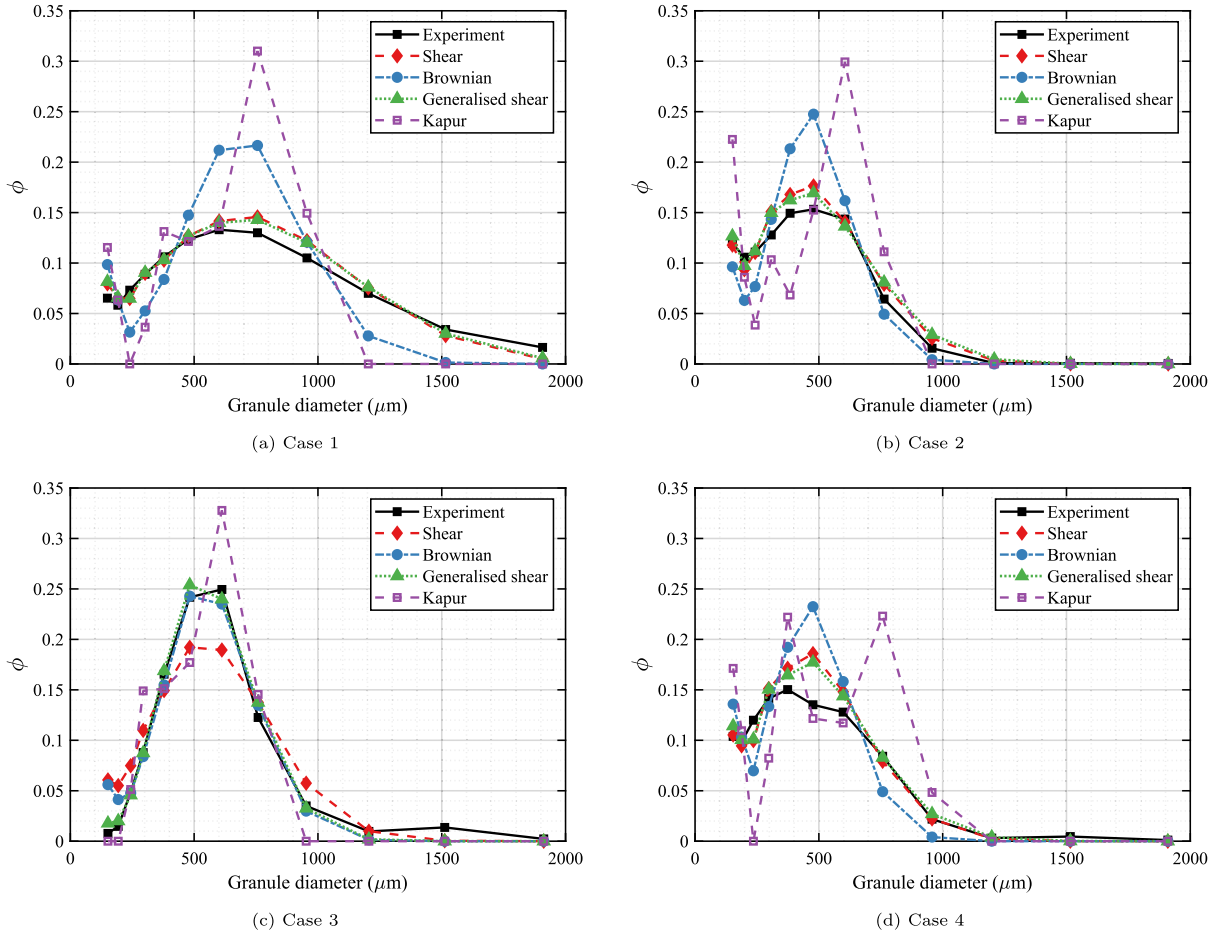

Fig. 13. Comparison of predicted and experimental granule size distributions (volume fraction vs. granule size) for Cases 1–4 using four aggregation kernels (shear, Brownian, generalised shear, and Kapur), with experimental measurements from Liu et al. [9].

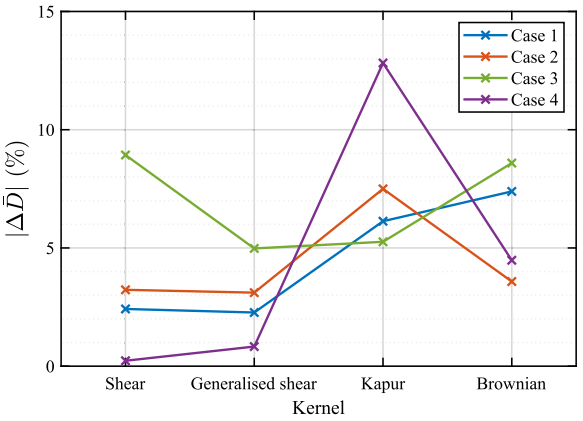

Fig. 14. Mean granule diameter difference, ΔD (%), for Cases 1–4 as a function of four aggregation kernels.

6. Conclusions

The present study developed a coupled 2D-CFD-PBM model to investigate the hydrodynamic behaviour and PSD evolution in SFBG. The scope of this work focuses on developing a computationally efficient reduced-order modelling framework capable

Table 7
Relative width comparison for different PBM kernels across all cases.

Case	Kernel	RW_*	RW	ΔRW (%)
Case 1	Shear	1.4009	1.3511	−3.55
	Generalised shear	1.4009	1.3942	−0.48
	Kapur	1.4009	1.1734	−16.24
	Brownian	1.4009	1.1986	−14.44
Case 2	Shear	1.1410	1.1406	−0.03
	Generalised shear	1.1410	1.2006	+5.23
	Kapur	1.1410	1.2382	+8.52
	Brownian	1.1410	0.9987	−12.47
Case 3	Shear	0.8397	1.0956	+30.47
	Generalised shear	0.8397	0.8507	+1.31
	Kapur	0.8397	0.7805	−7.05
	Brownian	0.8397	0.9806	+16.77
Case 4	Shear	1.1811	1.0957	−7.23
	Generalised shear	1.1811	1.2044	+1.97
	Kapur	1.1811	1.2748	+7.94
	Brownian	1.1811	1.0697	−9.43

RW_* denotes experimental values reported by Liu et al. [9]. (+) indicates overprediction, whereas (−) indicates underprediction relative to experiments.

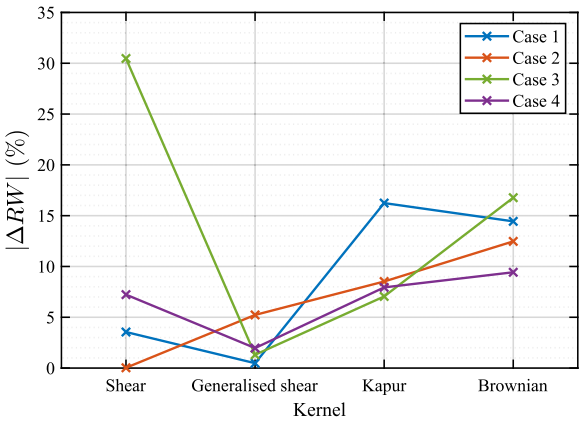

Fig. 15. Relative width difference, ΔRW (%), for Cases 1–4 as a function of four aggregation kernel.

of capturing the key hydrodynamic features of fluidisation and the dominant granulation mechanisms governing PSD evolution. The hydrodynamics of the fluidised bed were simulated using an Eulerian–Eulerian CFD formulation, while particle dynamics were represented using a two-compartment PBM solved through a finite-volume scheme. The integrated framework enabled simultaneous analysis of fluid flow behaviour and particle aggregation–breakage processes within the SFBG system. The 2D CFD simulations successfully reproduced the principal hydrodynamic characteristics of the fluidised bed, showing good agreement with both experimental [9] observations and previously reported 3D simulations [9]. The predicted ΔP closely matched the theoretical value, with a deviation of approximately 0.52 Pa, compared with a larger deviation of about 7.87 Pa in the corresponding 3D model. The difference in predicted ΔP between the 2D and 3D models remained relatively small throughout the simulation, with percentage differences of 2.22% at 0.1 s and 4.32% at 4 s. These results suggest that the reduced-order 2D formulation retained the system's essential hydrodynamic characteristics despite the absence of out-of-plane flow structures. The predicted bed expansion from the 2D model was also comparable to the 3D reference results. The H_{bed} discrepancy between the two models decreased from 5.1% in the initial stage to 2.66% at steady state, indicating that both modelling approaches converged to nearly the same final fluidisation behaviour.

The temporal evolution of the α_s captured the transition from the initial packed state to bubbling fluidisation and a statistically steady regime. Time-averaged results revealed realistic solids distribution patterns, including a denser lower region and a more dilute upper region, together with a core–annulus recirculation structure typical of bubbling fluidised beds. The coupled 2D CFD-based PBM successfully reproduced the overall shape and dominant size range of the experimentally observed PSD across all operating conditions. The hydrodynamic exchange information obtained from the CFD model proved sufficient for PBM-based granulation analysis. Among the aggregation kernels examined, the generalised shear kernel provided the most consistent overall agreement with the experimental PSDs, yielding balanced predictions of the $\overline{D}$ and RW, with deviations generally around 5% across the four cases. The shear kernel showed reasonable agreement in most cases but exhibited reduced accuracy under certain conditions. In contrast,

the Kapur kernel displayed excessive sensitivity on the coarse-particle side, while the Brownian kernel consistently underestimated the formation of larger granules. In conclusion, the findings of the present study indicate that the proposed 2D CFD two-compartment PBM captures the key global hydrodynamic trends and the PSD evolution of the SFBG, demonstrating reasonable agreement, while offering a computationally efficient reduced-order alternative to expensive 3D CFD–PBM simulations. Furthermore, the generalised kernel employed in the PBM exhibits superior fidelity relative to other kernels, aligning consistently with an alternative set of experimental data. In contrast, conventional model-based kernels documented in the literature inadequately represent the SFBG process.

Overall, the results of the present study demonstrate that the proposed 2D coupled CFD–PBM model effectively captures the key hydrodynamic and granulation phenomena in SFBG while maintaining satisfactory agreement with available experimental results and the previously coupled CFD–PBM model. The present model provides a computationally efficient reduced-order model suitable for preliminary analysis of SFBG systems and systematic evaluation of aggregation kernels. Future work should focus on extending the present model to incorporate additional physical mechanisms relevant to industrial granulation processes. In particular, integrating binder transport and moisture-dependent [59–62] particle properties into the PBM would improve the physical representation of granulation and drying phenomena.

Nomenclature

Symbol	Description
A_{DC}	Solids-weighted area of drying compartment
A_{WC}	Solids-weighted area of wetting compartment
$b(\cdot\|\cdot)$	Daughter size distribution function
$\bar{D}$	Mean granule diameter
H_{bed}	Bed height
M_0	Zeroth raw moment of the particle size distribution
M_1	First raw moment of the particle size distribution
n_{DC}	Number density function in drying compartment (DC)
n_{WC}	Number density function in wetting compartment (WC)
R	Particle exchange rate between WC and DC
S_{DC}	Breakage selection function in DC
S_0	Breakage rate constant
X, Y	Spatial coordinates/locations in the CFD flow domain
x, y	Particle volume coordinates in the PBM formulation
α_s	CFD-based solid volume fraction
β_{WC}	Aggregation kernel in WC
β_0	Aggregation rate constant
ΔP	Bed pressure drop
ΔP_{th}	Theoretical bed pressure drop
ϕ	Normalised volume-based size fraction
ϕ_i^{exp}	Experimental normalised volume-based size fraction in size class i
ϕ_i^{sim}	Simulated/predicted normalised volume-based size fraction in size class i
Abbreviations	
CFD	Computational fluid dynamics
DC	Drying compartment
PBM	Population balance model
PSD	Particle size distribution
SFBG	Spray fluidised bed granulation
WC	Wetting compartment

CRediT authorship contribution statement

Zeeshan Ansari: Writing – review & editing, Writing – original draft, Visualization, Validation, Investigation, Formal analysis, Conceptualization. **Mainendra Kumar Dewangan:** Writing – review & editing, Visualization, Validation, Investigation, Formal analysis, Conceptualization. **Ashok Das:** Writing – review & editing, Visualization, Validation, Methodology, Formal analysis, Conceptualization. **Stefan Heinrich:** Writing – review & editing, Visualization, Investigation, Formal analysis, Conceptualization. **Rohit Ramachandran:** Writing – review & editing, Validation, Investigation, Formal analysis, Conceptualization. **Mehakpreet Singh:** Writing – review & editing, Visualization, Validation, Supervision, Resources, Project administration, Methodology, Funding acquisition, Formal analysis, Conceptualization.

Declaration of competing interest

The authors declare that they have no known competing financial interests or personal relationships that could have appeared to influence the work reported in this paper.

Acknowledgements

First author Zeeshan Ansari gratefully recognises financial support from Taighde Éireann–Research Ireland under Grant number 18/CRT/6049. Author Ashok Das acknowledges funding received through the ANRF PM-ECRG scheme (File No.: ANRF/ECRG/2024/006104/PMS). For open access, the authors have applied a CC BY public copyright license to any Author Accepted Manuscript version arising from this submission.

Data availability

Data will be made available on request.

References

[1] Dilip M. Parikh, Handbook of pharmaceutical granulation technology, Drugs Sci. 81 (2005).
[2] Anneleen Burggraeve, Tinne Monteyne, Chris Vervaet, Jean Paul Remon, Thomas De Beer, Process analytical tools for monitoring, understanding, and control of pharmaceutical fluidized bed granulation: A review, Eur. J. Pharmaceut. Biopharmaceut. 83 (1) (2013) 2–15.
[3] Mehakpreet Singh, Saeed Shirazian, Vivek Ranade, Gavin M Walker, Ashish Kumar, Challenges and opportunities in modelling wet granulation in pharmaceutical industry–A critical review, Powder Technol. 403 (2022) 117380.
[4] Simon M Iveson, James D Litster, Karen Hapgood, Bryan J Ennis, Nucleation, growth and breakage phenomena in agitated wet granulation processes: A review, Powder Technol. 117 (1–2) (2001) 3–39.
[5] C. Bacher, P.M. Olsen, P. Bertelsen, J.M. Sonnergaard, Compressibility and compactibility of granules produced by wet and dry granulation, Int. J. Pharm. 358 (1–2) (2008) 69–74.
[6] Ashok Das, Jitendra Kumar, Population balance modeling of volume and time dependent spray fluidized bed aggregation kernel using Monte Carlo simulation results, Appl. Math. Model. 92 (2021) 748–769.
[7] Yinqiang Song, Tuo Zhou, Ruiqi Bai, Man Zhang, Hairui Yang, Assessment of the coating quality in a top-spray fluidized bed coater: An experimental study, Powder Technol. 439 (2024) 119663.
[8] Falah Alobaid, Naser Almohammed, Massoud Massoudi Farid, Jan May, Philip Rößger, Andreas Richter, Bernd Epple, Progress in CFD simulations of fluidized beds for chemical and energy process engineering, Prog. Energy Combust. Sci. 91 (2022) 100930.
[9] Huolong Liu, Ming Li, Two-compartmental population balance modeling of a pulsed spray fluidized bed granulation based on computational fluid dynamics (CFD) analysis, Int. J. Pharm. 475 (1–2) (2014) 256–269.
[10] Gurmeet Kaur, Mehakpreet Singh, Themis Matsoukas, Jitendra Kumar, Thomas De Beer, Ingmar Nopens, Two-compartment modeling and dynamics of top-sprayed fluidized bed granulator, Appl. Math. Model. 68 (2019) 267–280.
[11] Gero Stoeckl, Stefan Bellinghausen, Stefan Heinrich, DEM informed surrogate modelling for PBM in fluidized beds, Chem. Eng. J. (2025) 171940.
[12] Mirko Peglow, Jitendra Kumar, Stefan Heinrich, Gerald Warnecke, Evangelos Tsotsas, Lothar Mörl, Bertram Wolf, A generic population balance model for simultaneous agglomeration and drying in fluidized beds, Chem. Eng. Sci. 62 (1–2) (2007) 513–532.
[13] I.T. Cameron, F.Y. Wang, C.D. Immanuel, F. Stepanek, Process systems modelling and applications in granulation: A review, Chem. Eng. Sci. 60 (14) (2005) 3723–3750.
[14] Matthias Börner, Andreas Bück, Evangelos Tsotsas, DEM-CFD investigation of particle residence time distribution in top-spray fluidised bed granulation, Chem. Eng. Sci. 161 (2017) 187–197.
[15] Jayanta Chakraborty, Jitendra Kumar, Mehakpreet Singh, Alan Mahoney, Doraiswami Ramkrishna, Inverse problems in population balances. Determination of aggregation kernel by weighted residuals, Ind. Eng. Chem. Res. 54 (42) (2015) 10530–10538.
[16] Nageswara Rao Narni, Mirko Peglow, Gerald Warnecke, Jitendra Kumar, Stefan Heinrich, JAM Kuipers, Modeling of aggregation kernels for fluidized beds using discrete particle model simulations, Particuology 13 (2014) 134–144.
[17] Eric Otto, Robert Dürr, Gerd Strenzke, Stefan Palis, Andreas Bück, Evangelos Tsotsas, Achim Kienle, Kernel identification in continuous fluidized bed spray agglomeration from steady state data, Adv. Powder Technol. 32 (7) (2021) 2517–2529.
[18] Jingyuan Sun, Yefeng Zhou, Congjing Ren, Jingdai Wang, Yongrong Yang, CFD simulation and experiments of dynamic parameters in gas–solid fluidized bed, Chem. Eng. Sci. 66 (21) (2011) 4972–4982.
[19] Mohsen Shiea, Antonio Buffo, Marco Vanni, Daniele Marchisio, Numerical methods for the solution of population balance equations coupled with computational fluid dynamics, Annu. Rev. Chem. Biomol. Eng. 11 (1) (2020) 339–366.
[20] Naghmeh Abedi, Mohsen Nasr Esfahany, Experimental and CFD-PBM study on fluidization behavior of fine cohesive powder in a pulsed fluidized bed, Ind. Eng. Chem. Res. 64 (35) (2025) 17195–17216.
[21] Paul Kieckhefen, Swantje Pietsch-Braune, Stefan Heinrich, Product-property guided scale-up of a fluidized bed spray granulation process using the CFD-DEM method, Processes 10 (7) (2022) 1291.
[22] Christian Drumm, Menwer M. Attarakih, Hans-Jörg Bart, Coupling of CFD with DPBM for an RDC extractor, Chem. Eng. Sci. 64 (4) (2009) 721–732.
[23] Kunyu Guo, Tiefeng Wang, Yefei Liu, Jinfu Wang, CFD-PBM simulations of a bubble column with different liquid properties, Chem. Eng. J. 329 (2017) 116–127.
[24] João Cardoso, Valter Silva, Daniela Eusébio, Paulo Brito, Ronney Mancebo Boloy, Luís Tarelho, José Luz Silveira, Comparative 2D and 3D analysis on the hydrodynamics behaviour during biomass gasification in a pilot-scale fluidized bed reactor, Renew. Energy 131 (2019) 713–729.
[25] Ashok Das, Jean-Sébastien Kroll-Rabotin, Thibault Quatravaux, Jean-Pierre Bellot, Investigating chemical heterogeneity in inclusion populations: A multivariate population balance model study in gas-stirred ladles, Ind. Eng. Chem. Res. 62 (48) (2023) 20789–20801.
[26] Junwei Su, Zhaolin Gu, Yun Li, Shiyu Feng, X. Yun Xu, Solution of population balance equation using quadrature method of moments with an adjustable factor, Chem. Eng. Sci. 62 (21) (2007) 5897–5911.
[27] Sanjeev Kumar, Doraiswami Ramkrishna, On the solution of population balance equations by discretization—I. A fixed pivot technique, Chem. Eng. Sci. 51 (8) (1996) 1311–1332.
[28] M.J. Hounslow, R.L. Ryall, V.R. Marshall, A discretized population balance for nucleation, growth, and aggregation, AIChE J. 34 (11) (1988) 1821–1832.

[29] Antonio Buffo, Daniele L Marchisio, Marco Vanni, Peter Renze, Simulation of polydisperse multiphase systems using population balances and example application to bubbly flows, Chem. Eng. Res. Des. 91 (10) (2013) 1859–1875.
[30] Jay Sanyal, Daniele L Marchisio, Rodney O Fox, Kumar Dhanasekharan, On the comparison between population balance models for CFD simulation of bubble columns, Ind. Eng. Chem. Res. 44 (14) (2005) 5063–5072.
[31] Mehakpreet Singh, Jitendra Kumar, Andreas Bück, A volume conserving discrete formulation of aggregation population balance equations on non-uniform meshes, IFAC-PapersOnLine 48 (1) (2015) 192–197.
[32] Hugh M. Hulburt, Stanley Katz, Some problems in particle technology: A statistical mechanical formulation, Chem. Eng. Sci. 19 (8) (1964) 555–574.
[33] Robert McGraw, Description of aerosol dynamics by the quadrature method of moments, Aerosol Sci. Technol. 27 (2) (1997) 255–265.
[34] Daniele L. Marchisio, Rodney O. Fox, Solution of population balance equations using the direct quadrature method of moments, J. Aerosol Sci. 36 (1) (2005) 43–73.
[35] Vahid Akbari, Tohid Nejad Ghaffar Borhani, Ahmad Shamiri, Roya Aramesh, Mohamed Azlan Hussain, Mohd Kamaruddin Abd Hamid, 2D CFD-PBM simulation of hydrodynamic and particle growth in an industrial gas phase fluidized bed polymerization reactor, Chem. Eng. Res. Des. 104 (2015) 53–67.
[36] Daniele L. Marchisio, Rodney O. Fox, Computational Models for Polydisperse Particulate and Multiphase Systems, Cambridge University Press, 2013.
[37] Louis Forestier-Coste, Simona Mancini, A finite volume preserving scheme on nonuniform meshes and for multidimensional coalescence, SIAM J. Sci. Comput. 34 (6) (2012) B840–B860.
[38] Mehakpreet Singh, Jitendra Kumar, Andreas Bück, Evangelos Tsotsas, An improved and efficient finite volume scheme for bivariate aggregation population balance equation, J. Comput. Appl. Math. 308 (2016) 83–97.
[39] Mehakpreet Singh, Vivek Ranade, Orest Shardt, Themis Matsoukas, Challenges and opportunities concerning numerical solutions for population balances: A critical review, J. Phys. A 55 (38) (2022) 383002.
[40] Mehakpreet Singh, Hamza Y Ismail, Randhir Singh, Ahmad B Albadarin, Gavin Walker, Finite volume approximation of nonlinear agglomeration population balance equation on triangular grid, J. Aerosol Sci. 137 (2019) 105430.
[41] Mehakpreet Singh, Jayanta Chakraborty, Jitendra Kumar, Ramini Ramakanth, Accurate and efficient solution of bivariate population balance equations using unstructured grids, Chem. Eng. Sci. 93 (2013) 1–10.
[42] Mubashir Hussain, Jitendra Kumar, Mirko Peglow, Evangelos Tsotsas, On two-compartment population balance modeling of spray fluidized bed agglomeration, Comput. Chem. Eng. 61 (2014) 185–202.
[43] Dimitri Gidaspow, Multiphase Flow and Fluidization: Continuum and Kinetic Theory Descriptions, Academic Press, Boston, MA, ISBN: 978-0-12-282470-8, 1994.
[44] C.K.K. Lun, S.B. Savage, D.J. Jeffrey, N. Chepurniy, Kinetic theories for granular flow: Inelastic particles in couette flow and slightly inelastic particles in a general flowfield, J. Fluid Mech. 140 (1984) 223–256.
[45] B.G.M. Van Wachem, J.C. Schouten, C.M. Van den Bleek, R. Krishna, J.L. Sinclair, Comparative analysis of CFD models of dense gas–solid systems, AIChE J. 47 (5) (2001) 1035–1051.
[46] Teresa Jiménez, Christelle Turchiuli, Elisabeth Dumoulin, Particles agglomeration in a conical fluidized bed in relation with air temperature profiles, Chem. Eng. Sci. 61 (18) (2006) 5954–5961.
[47] Christelle Turchiuli, T. Jimenèz, E. Dumoulin, Identification of thermal zones and population balance modelling of fluidized bed spray granulation, Powder Technol. 208 (2) (2011) 542–552.
[48] Huolong Liu, Mingzhong Li, Population balance modelling and multi-stage optimal control of a pulsed spray fluidized bed granulation, Int. J. Pharm. 468 (1–2) (2014) 223–233.
[49] M.V. Smoluchowski, Mathematical theory of the kinetics of the coagulation of colloidal solutions, Z. Phys. Chem. 92 (1917) 129–168.
[50] A. Ding, M.J. Hounslow, C.A. Biggs, Population balance modelling of activated sludge flocculation: Investigating the size dependence of aggregation, breakage and collision efficiency, Chem. Eng. Sci. 61 (1) (2006) 63–74.
[51] P.C. Kapur, Kinetics of granulation by non-random coalescence mechanism, Chem. Eng. Sci. 27 (10) (1972) 1863–1869.
[52] Vasyl Skorych, Maksym Dosta, Ernst-Ulrich Hartge, Stefan Heinrich, Robin Ahrens, Sabine Le Borne, Investigation of an FFT-based solver applied to dynamic flowsheet simulation of agglomeration processes, Adv. Powder Technol. 30 (3) (2019) 555–564.
[53] Rainer Storn, Kenneth Price, Differential evolution–A simple and efficient heuristic for global optimization over continuous spaces, J. Global Optim. 11 (4) (1997) 341–359.
[54] Richard H. Byrd, Peihuang Lu, Jorge Nocedal, Ciyou Zhu, A limited memory algorithm for bound constrained optimization, SIAM J. Sci. Comput. 16 (5) (1995) 1190–1208.
[55] Hongbo Shi, Alexandra Komrakova, Petr Nikrityuk, Fluidized beds modeling: Validation of 2D and 3D simulations against experiments, Powder Technol. 343 (2019) 479–494.
[56] David Escudero, Theodore J. Heindel, Bed height and material density effects on fluidized bed hydrodynamics, Chem. Eng. Sci. 66 (16) (2011) 3648–3655.
[57] D.C. Sau, Swati Mohanty, K.C. Biswal, Minimum fluidization velocities and maximum bed pressure drops for gas–solid tapered fluidized beds, Chem. Eng. J. 132 (1–3) (2007) 151–157.
[58] Shijiao Li, Peng Zhao, Ji Xu, Li Zhang, Junwu Wang, Direct comparison of CFD-DEM simulation and experimental measurement of Geldart A particles in a micro-fluidized bed, Chem. Eng. Sci. 242 (2021) 116725.
[59] Dana Barrasso, Arwa El Hagrasy, James D Litster, Rohit Ramachandran, Multi-dimensional population balance model development and validation for a twin screw granulation process, Powder Technol. 270 (2015) 612–621.
[60] Tarun De, Ashley Dan, Rohit Ramachandran, Ashok Das, An adaptive and bi-directional PBM-dem framework for multi-component wet granulation: Bridging the gap between computational efficiency and high-fidelity model physics, Powder Technol. (2025) 121507.
[61] Saeed Shirazian, Hamza Y Ismail, Mehakpreet Singh, Rahamatullah Shaikh, Denise M Croker, Gavin M Walker, Multi-dimensional population balance modelling of pharmaceutical formulations for continuous twin-screw wet granulation: Determination of liquid distribution, Int. J. Pharm. 566 (2019) 352–360.
[62] Hamza Y Ismail, Mehakpreet Singh, Ahmad B Albadarin, Gavin M Walker, Complete two dimensional population balance modelling of wet granulation in twin screw, Int. J. Pharm. 591 (2020) 120018.